Mass transfer between fluids as a mechanism for seismic wave attenuation: Experimental evidence from water-CO2 saturated sandstones

Samuel Chapman, Jan Borgomano, Beatriz Quintal, Sally Benson, Jerome Fortin

Geophysical Journal International

Geophys. J. Int. (2022) **230,** 216–234
Advance Access publication 2022 February 21
GJI Rock and Mineral Physics, Rheology

https://doi.org/10.1093/gji/ggac067

Mass transfer between fluids as a mechanism for seismic wave attenuation: experimental evidence from water–CO_2 saturated sandstones

Samuel Chapman [1,2,3,*] Jan V. M. Borgomano,[1] Beatriz Quintal,[2] Sally M. Benson[3] and Jerome Fortin[1]

[1] *Laboratoire de Géologie, Ecole Normale Supérieure/CNRS UMR* 8538*, PSL Research University,* 75006 *Paris, France E-mail: samuel.chapman38@gmail.com*
[2] *Institute of Earth Sciences, University of Lausanne, Lausanne CH-*1015*, Switzerland*
[3] *Department of Energy Resources Engineering, Stanford University, Stanford, CA* 94305*, USA*

Accepted 2022 February 11. Received 2022 February 5; in original form 2021 October 6

SUMMARY

Seismic waves are typically assumed to propagate fast enough through a porous rock saturated with multiple fluid phases such that the interaction between the fluids can be considered adiabatic, or thermodynamically unrelaxed. However, at low gas saturations and when the gas is present in the form of microscopic bubbles the fluid mixture may in fact be thermodynamically relaxed at seismic frequencies. The effective fluid is then significantly more compressible. A transition from a thermodynamically relaxed to unrelaxed state of the fluids will be accompanied by frequency dependent attenuation of the wave in response to heat and/or mass transfer. We conducted experiments on two partially saturated sandstone samples to measure frequency dependent attenuation and modulus dispersion at seismic frequencies (<1000 Hz). For CO_2 saturations of 0.1–0.2 per cent we observe significant attenuation and dispersion in the bulk and shear modulus, with an attenuation peak at ∼100 Hz. The bulk modulus was significantly lower than the prediction by Gassmann–Wood fluid substitution, which assumes that the fluids are thermodynamically unrelaxed. Numerical simulations in poroelastic media further indicate that a partially drained boundary condition does not adequately explain the observed attenuation and dispersion, particularly in the shear modulus. Numerical simulations at the microscopic scale support the notion that pore-scale heterogeneities could explain the observed shear attenuation and dispersion, since an external shear deformation can cause local compressions of the pore space. The observed attenuation and dispersion are interpreted to be predominantly due to a transition from a thermodynamically relaxed to unrelaxed state of the saturating fluids.

Key words: Elasticity and anelasticity; Numerical modelling; Seismic attenuation; Microstructures.

1 INTRODUCTION

In porous rocks saturated with fluids of different phases the intrinsic attenuation and dispersion of waves at seismic frequencies (<1000 Hz) is typically attributed to fluid pressure diffusion (FPD), either at the meso- or microscopic scale (e.g. Pride *et al*. 2004; Müller *et al*. 2010). FPD arises from the contrast in compressibility between different fluid phases or between more and less compliant constituents of the porous material, such as between grain contacts and isometric pores. For porous rocks saturated with multiple fluid phases it is typically assumed that seismic waves propagate fast enough through the medium so that the interaction between the fluids can be considered adiabatic (e.g. Batzle & Wang 1992), that is, there is no heat or mass transfer between the fluids. However, this assumption may not hold at low gas saturation and if the bubble size is very small. At low enough frequencies the fluids are in thermodynamic equilibrium and are significantly more compressible compared to when the interaction between them can be considered adiabatic (e.g. Kiefer 1977). A transition, where the fluids go from thermodynamically relaxed to unrelaxed with increasing frequency, will be accompanied by significant energy dissipation. Better understanding under what conditions the assumption of adiabatic interaction between fluid

*Now at: Ecole Normale Supérieure, Paris.

phases breaks down is important in the context of seismic monitoring because it could lead, for example, to an overestimation of gas content in a reservoir (Khalid *et al*. 2014; Blanchard & Delommot 2015).

The impact of mass and heat transfer on the attenuation and dispersion of waves has been widely investigated. Kiefer (1977) and Landau & Lifshitz (1989) derived limiting expressions for the effective fluid velocity. A number of models for the frequency dependent attenuation of waves in liquids containing small gas bubbles have been proposed to account for heat and mass transfer (e.g. Mecredy & Hamilton 1972; Onuki 1991; Prosperetti 2015; Fuster & Montel 2015). Auriault *et al*. (2002) derived wave equations for a porous material saturated with a fluid containing diffuse gas bubbles and accounted for capillary, heat and phase change effects. Grab *et al*. (2017) recently utilized the model by Fuster & Montel (2015) for the frequency dependent compressibility of a pure fluid containing vapour bubbles in numerical simulations solving Biot's (1941) quasistatic equations of poroelasticity to better understand the attenuation and dispersion of seismic waves in a fractured geothermal reservoir. Coste & Laroche (1993) experimentally investigated the acoustic response in a bubble-liquid mixture of diethyl-ether and concluded that their observation of very low wave velocities could only be explained by considering phase changes effects.

Only a handful of studies have experimentally investigated the impact of small amounts of gas ($\leq$1 per cent) on the modulus dispersion and attenuation at seismic frequencies in otherwise water saturated porous rocks. Such small amounts of gas were introduced into the initially water saturated samples by reducing the pore pressure and allowing the dissolved gas to come out of solution. Using this method, frequency dependent attenuation and dispersion in the Young's modulus were observed in multiple Berea sandstone samples and a Borosilicate sample in the frequency range between 1 and 10 Hz (Tisato *et al*. 2015; Chapman *et al*. 2017; Chapman *et al*. 2018). These experiments were performed with the same experimental setup, at room temperature and at pore pressures under 1 MPa. Tisato *et al*. (2015) attributed the observations to the exsolution and dissolution of homogeneously distributed pore scale gas bubbles in response to the pore pressure oscillation and they used a corresponding numerical model to solve for the frequency dependent effective fluid bulk modulus. Similar experiments on Berea sandstone samples were performed by Spencer & Shine (2016) and Chapman *et al*. (2021), at $\sim$2.4 and $\sim$1 MPa pore pressure, respectively. For low gas saturations, both however observe frequency dependent attenuation only at frequencies $>$100 Hz. In addition, Chapman *et al*. (2021) utilized X-ray computed tomography (CT) to investigate the CO_2 distribution following exsolution and observed that most of the CO_2 came out of solution near the sample outlet, where the pore pressure drop was initiated, resulting in a heterogenous distribution of the water and gas along the sample length. The observed fluid distribution contradicts the assumption of a homogenous distribution of pore scale gas bubbles made by Tisato *et al*. (2015) and Chapman *et al*. (2017, 2018). Based both on a qualitative and quantitative analysis Chapman *et al*. (2021) attributed their observations to mesoscopic scale fluid pressure diffusion due to a heterogenous distribution of CO_2.

The drawback of the studies by Tisato *et al*. (2015) and Chapman *et al*. (2017, 2018) is the relatively low pore pressure at which the experiments were performed. With Gassmann (1951) fluid substitution and the adiabatic effective bulk modulus of the fluid mixture given by Wood's (1955) equation, it can be shown that at 1 per cent gas saturation the undrained bulk modulus of the samples can be on the order of the drained one. Consequently, the impact of mass and heat transfer would be negligible. To address this drawback, we performed exsolution experiments on two sandstone samples, a Berea and a Domengine, with CO_2 and water as the operating fluids at higher pressure and temperatures. Forced oscillation measurements, in the frequency range between 0.1 and 1000 Hz, were performed on the partially saturated samples at 5 and 9 MPa pore pressure, at 45 °C, to investigate gaseous and supercritical CO_2, respectively. With the Domengine sample we also performed exsolution experiments in combination with X-ray CT to investigate the fluid distribution. The following sections will cover: (i) in greater detail the theory behind thermodynamically relaxed and unrelaxed fluid mixtures, (ii) the experimental methodology, (iii) the experimental results and (iv) the analysis of the observations with the help of mesoscopic poroelastic and micro-mechanical numerical simulations. Finally, we will discuss the broader implications of our findings and present our conclusions.

2 THEORY

2.1 Fluid substitution with relaxed and unrelaxed fluids

Gassmann's (1951) equations are widely used to relate the drained mechanical properties of a porous rock to its undrained mechanical properties. Gassmann assumes that the rock matrix is composed of a solid homogenous mineral material and that the saturating fluids do not chemically react with the mineral material (e.g. Mavko *et al*. 2009). Furthermore, the pore pressure is assumed to be equilibrated throughout the representative elementary volume (REV), meaning that the frequency of the pressure perturbation is low enough to allow enough time for the fluids to flow so that there will be no pore pressure gradients. For a mechanically isotropic rock Gassmann's (1951) equations take the following form:

$$K_u = K_d + \frac{(1 - K_d/K_s)^2}{\phi/K_f + (1-\phi)/K_s - K_d/K_s^2}, \tag{1}$$

$$G_u = G_d, \tag{2}$$

where ϕ is the porosity, K_u and G_u are the undrained bulk and shear moduli, K_d and G_d are the drained bulk and shear moduli, K_s and K_f are the bulk moduli of the solid matrix and of the pore fluid, respectively. An important result of Gassmann's (1951) derivations is that the shear modulus is not impacted by the presence of a fluid in the pore space (eq. 2,e.g. Berrymann 1999).

For rocks saturated with multiple fluids the common extensions of Gassmann's equations are the high frequency Gassmann–Hill limit and low frequency Gassmann–Wood (GW) limit (e.g. Toms *et al*. 2006). Inherent in the Gassmann–Hill limit is that the frequency is high enough such that the fluids behave as if they were isolated (Mavko & Mukerji 1998). The following discussion will therefore focus on the assumptions of the GW limit, which uses a Reuss average to express an effective fluid bulk modulus, referred to as Wood's (1955) approximation:

$$K_W = \left(\frac{S_g}{K_g} + \frac{S_l}{K_l} \right)^{-1}, \tag{3}$$

where K_g and K_l are the adiabatic bulk moduli of the gas and liquid, respectively. S_g and S_l are the gas and liquid saturations, such that $S_g + S_l = 1$. Wood's (1955) approximation assumes that (i) the pressure in the two fluid phases is equal and (ii) that there is no heat and mass transfer between them. As with Gassmann's equations, the frequency needs to be low enough for the fluid pressure to be equilibrated throughout the medium, which in other words means

that the spatial scale of the fluid heterogeneities must be small compared to the seismic wavelength. Conversely, the second Wood's assumption holds when the frequency is high enough such that there is not enough time for mass and heat exchange to occur between the phases. If the gas phase heterogeneity is very small the second assumption no longer holds. For such a case Landau & Lifshitz (1989) determined a low frequency approximation for the sonic velocity of a thermodynamically relaxed fluid:

$$c_{\mathrm{LL}} = \frac{\Delta H_{\mathrm{evap}} \mu P V_{\mathrm{l}}}{RT\left(C_{p_{\mathrm{l}}} T\right)^{1/2}}, \tag{4}$$

where ΔH_{evap} is the enthalpy of vapourization, defined as the difference between the vapour and liquid enthalpies or $\Delta H_{\mathrm{evap}} = H_{\mathrm{v}} - H_{\mathrm{l}}$, μ is the molar mass, P is pressure, V_{l} is the liquid's specific volume, R is the gas constant, $C_{P_{\mathrm{l}}}$ is the liquid heat capacity and T is the absolute temperature. The bulk modulus of the thermodynamically relaxed fluid can be determined as:

$$K_{\mathrm{LL}} = \frac{c_{\mathrm{LL}}^2}{V_{\mathrm{l}}}. \tag{5}$$

Eq. (4) is an approximation strictly applicable to a pure fluid with a liquid and vapour phase, where the liquid only contains a small amount of vapour in the form of diffuse bubbles. The analysis of Landau & Lifshitz (1989) has been extended to multicomponent fluids using a variety of approaches (e.g. Picard & Bishnoi 1987; Firoozabadi & Pan 2000; Nichita *et al*. 2010; Khalid *et al*. 2014). Both the thermodynamically relaxed (eq. 5) and unrelaxed fluid bulk moduli (eq. 3) can be inserted instead of the single-phase fluid bulk modulus K_{f} in Gassmann's equation (eq. 1) to describe a partially saturated and undrained porous rock. At low gas saturations the bulk modulus of thermodynamically relaxed fluids can be significantly lower than the bulk modulus of the unrelaxed fluids as determined by Wood's (1955) approximation (e.g. Khalid *et al*. 2014). In the seismic frequency range (<1000 Hz) this could result in significant dispersion in the mechanical stiffness of the partially saturated rock as well as frequency dependent attenuation of seismic waves propagating in such a medium.

2.2 Frequency dependent attenuation and dispersion

The frequency dependent attenuation and stiffness modulus dispersion mentioned at the end of the previous section is a result of time dependent mass and heat diffusion. For pure two-phase fluids Onuki (1991) derived an expression for the frequency dependent adiabatic bulk modulus that reduces to the Landau–Lifshitz bulk modulus at low frequencies and Wood's approximation at high frequencies. Prosperetti (2015) and Fuster & Montel (2015), recently also derived expressions for the frequency dependent compressibility of liquids containing vapour bubbles.

For non-pure fluids, Tisato *et al*. (2015) explained laboratory measurements using the frequency dependent attenuation and dispersion associated with the exsolution and dissolution of a gas bubble in water (Figs 1a and b), for which they solved the rate of change of dissolved gas mass and the associated rate of change in the bubble radius (Holocher *et al*. 2003; Liang *et al*. 2011):

$$\frac{\mathrm{d}n}{\mathrm{d}t} = 4\pi r D_{\mathrm{w}} \left(c_{\mathrm{w}} - \frac{1}{K_{\mathrm{H}}} \left(P_{\mathrm{f}} + \frac{2\sigma}{r} \right) \right) \text{and,} \tag{6}$$

$$\frac{\mathrm{d}r}{\mathrm{d}t} = \left(\frac{3RT}{4\pi r} \frac{\mathrm{d}n}{\mathrm{d}t} - r^2 \frac{\mathrm{d}P_{\mathrm{f}}}{\mathrm{d}t} \right) \frac{1}{4\sigma + 3r P_{\mathrm{f}}}, \tag{7}$$

where n is the mass of gas being dissolved, r is the bubble radius, D_{w} is the diffusion coefficient, c_{w} is the concentration of dissolved gas in the water, K_H is Henry's law constant, P_{f} is the time dependent fluid pressure such that $P_{\mathrm{f}} = P + P_a \sin(2\pi f t)$, σ is the surface tension and R and T are again the gas constant and temperature, respectively. Eq. (6) is derived from the proportionality between the interphase mass flux and the concentration gradient in the water and assumes that there is no flow and that the bubble radius is large compared to the thickness of the water shell around the bubble where diffusion dominates (Holocher *et al*. 2003). Eq. (7) is derived from the differentiation of the ideal gas law with respect to time (Liang *et al*. 2011). A Euler finite difference scheme is used to solve eqs (6) and (7) in the work of Tisato *et al*. (2015). The updated bubble radius and the elastic deformation of the water are then used to find the total volumetric strain. The time dependent volumetric strain and pressure are converted into the frequency domain using a discrete Fourier transform. Finally, a complex frequency dependent fluid bulk modulus is determined as:

$$K_{\mathrm{f}}^* = \frac{P_{\mathrm{f}}}{\epsilon_{\mathrm{vol}}}, \tag{8}$$

where ϵ_{vol} is the complex and frequency dependent total volumetric strain. The associated attenuation is (O'Connell & Budiansky 1978; Masson & Pride 2014):

$$Q^{-1} = \frac{Im\left(K_{\mathrm{f}}^*\right)}{Re\left(K_{\mathrm{f}}^*\right)}. \tag{9}$$

Fig. 1(b) shows the frequency dependent fluid bulk modulus and the associated attenuation determined by solving eqs (6) and (7) for a CO_2 gas bubble with a radius of 5 μm, surrounded by a shell of water (Fig. 1a), such that the gas saturation is ∼0.2 per cent, at a pressure of 5 MPa and a temperature of 45 °C. The fluid properties are listed in Table 1. The model results converge approximately, with a difference of ∼1 MPa, to both the Landau–Lifshitz limit (eq. 5) at low frequencies and to the Wood limit (eq. 3) at high frequencies. For the Wood approximation the isothermal bulk modulus of CO_2 is used because the model assumes isothermal conditions. The causality between the fluid bulk modulus dispersion and attenuation is verified with the Kramers–Kronig (KK) relations (e.g. Mavko *et al*. 2009). The characteristic frequency, where attenuation is maximal, in the case of heat transfer is governed by the thermal diffusion length in the liquid phase (Onuki 1991). Similarly, for the case of mass transfer the characteristic frequency is governed by diffusion length of the gas in the fluid phase and can be defined (Khalid *et al*. 2014) as:

$$f_{\mathrm{c}} = \frac{D_{\mathrm{w}} S_{\mathrm{g}}^{2/3}}{r^2}. \tag{10}$$

For the parameters used in this example, we find a characteristic frequency of 2.4 Hz, which is consistent with the results presented in Fig. 1(b). The complex fluid bulk modulus can be substituted into Gassmann's (1951) equation (eq. 1) to determine the complex bulk modulus of the partially saturated rock. Fig. 1(c) shows the frequency dependent bulk modulus and attenuation of the saturated rock, in this case utilizing the properties of a Berea sandstone sample (Table 2). Again, the model bulk modulus converges to the GLL limit at low frequencies, which is on the order of the drained bulk modulus of the rock, and at high frequencies to the GW limit. The attenuation in the saturated rock (∼0.07) is reduced compared to that of the effective fluid (∼5), however, still significant.

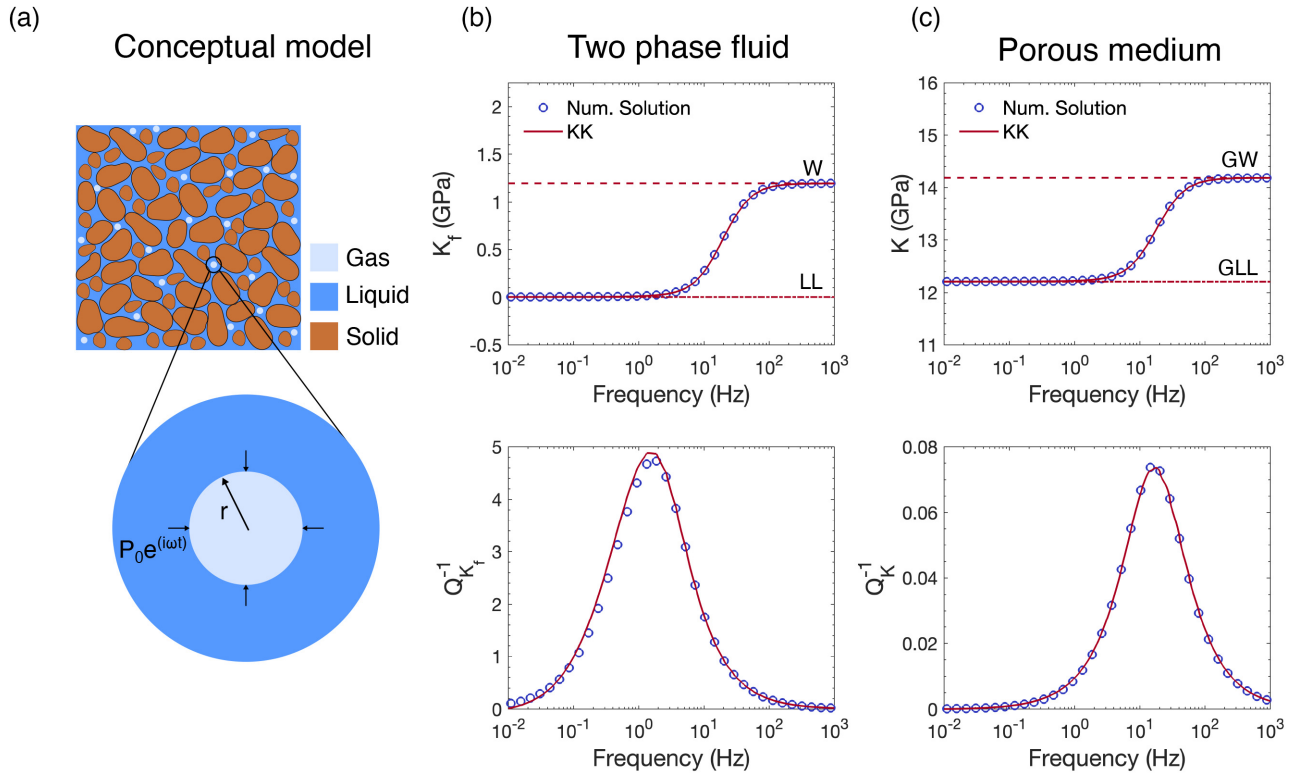

Figure 1. (a) Conceptual illustration of a homogeneously distributed gas phase in a porous medium subject to an oscillating pressure. (b) The frequency dependent fluid bulk modulus K_f and the associated attenuation Q_{Kf}^{-1} in response to the exsolution–dissolution of the gas phase in the surrounding water. Included are the bulk modulus of the relaxed fluid at low frequencies according to Landau & Lifshitz (1989) (LL) and the effective fluid bulk modulus according to Wood's (1955) relation (W). (c) The frequency dependent bulk modulus K and attenuation Q_K^{-1} of the corresponding partially saturated porous medium using Gassmann's (1951) fluid substitution. Included are the Gassmann–Landau–Lifshitz limit (GLL) for the relaxed fluids and the Gassmann–Wood limit (GW) for the unrelaxed fluids. The results of the Kramers–Kronig relations KK confirm the causality between the modulus dispersion and attenuation. The exsolution–dissolution model is solved for a bubble with a radius of 5 μm, a gas saturation of ∼0.2 per cent at a pore pressure of 5 MPa and a temperature of 45 °C. The fluid properties are given in Table 1 and the rock properties are those of the Berea sandstone (BSP4), given in Table 2.

3 EXPERIMENTAL METHODOLOGY

3.1 Dynamic stress and strain

To measure the frequency dependent attenuation (Q^{-1}) and modulus dispersion the samples are subjected to forced oscillations in a tri-axial cell, at ENS Paris. The frequency of the axial oscillations ranges from less than 1 Hz up to 1000 Hz. The axial and radial deformation of the samples are measured with four bi-axial 350 Ω foil gauges (TML FCB-6-350-11). The axial stress is inferred from the elastic deformation of the aluminium end plate. The axial stress amplitude of 0.2–0.4 MPa produces axial ϵ_{ax} and radial ϵ_{rad} strain amplitudes of $\sim 10^{-5}$ to $\sim 10^{-6}$, respectively. A minimum of 50 sinusoidal stress cycles per frequency are applied to the samples. The time dependent stress and strain signals for each frequency are averaged and a Fourier transform is used to determine their phase angles and amplitude. From the axial and radial strain amplitudes the sample's Poisson ratio ν and Young's modulus E are determined. The attenuation associated with each modulus is determined from the phase shift between the stress and strains (O'Connell & Budiansky 1978). In addition to axial oscillations, the confining pressure can be oscillated at frequencies below 1 Hz. From the hydrostatic oscillations and the volumetric strain, defined as $\epsilon_{\text{vol}} = \epsilon_{ax} + 2\epsilon_{\text{rad}}$, the bulk modulus and attenuation can be determined. Microvalves in the top and bottom sample holders allow for measurements to be performed under drained and undrained boundary conditions. These valves reduce the remaining volume of the fluid lines connected to the sample to ∼30 μl. Borgomano *et al*. (2020) provides a detailed description of the tri-axial cell, data processing and calibration.

3.2 X-ray CT imaging

X-ray images of the samples were taken with a medical computed tomography scanner (General Electric Hi-Speed CT), at Stanford University. All scans were performed at a tube current of 200 mA, a radiation energy level of 120 keV and a field of view of 9.6 cm, giving an initial pixel resolution of 0.1875 × 0.1875 mm^2. The porosity and CO_2 saturation are determined with the X-ray saturation method, by combining scans of the sample saturated with different fluids (e.g. Akin & Kovscek 2003). For the analysis of the porosity and fluid saturation the average of 3 repeated scans are used and the pixels are coarsened to 1.5 × 1.5 mm^2, which allows for reducing the uncertainty in the voxel scale porosity and fluid saturation to ±0.5 and ±2 per cent abs., respectively. The experiments were carried out with the same core-flooding setup used by Krevor *et al*. (2012).

3.3 Sample description and preparation

Experiments were performed on a Domengine sandstone sample taken from a gallery at the Black Diamond Mine Regional Park

Table 1. Fluid properties.

Symbol	Property	Value
K_g	Isothermal CO_2 bulk modulus (GPa)	5×10^{-3}
K_l	Adiabatic Water bulk modulus (GPa)	2.37 [a]
η_g	CO_2 viscosity (Pa × s)	1.72×10^{-5} [a]
η_l	Water viscosity (Pa × s)	6×10^{-4} [a]
σ	Surface tension (N m^{-1})	0.045 [b]
T	Temperature (K)	318.15
K_H	Henry's law constant (Pa m^3 mol^{-1})	4878.5 [c]
D_w	Diffusion coefficient (m^2 s^{-1})	3.643×10^{-9} [d]
C_p	CO_2 heat capacity, constant pressure [J (kg K)$^{-1}$]	1400.1 [a]
C_v	CO_2 heat capacity, constant volume [J (kg K)$^{-1}$]	798.4 [a]
C_{pl}	Water heat capacity, constant pressure [J (kg K)$^{-1}$]	4168.7 [a]
V_l	Water specific volume (m^3 kg^{-1})	0.0010077 [a]
H_l	Water liquid enthalpy (J kg^{-1})	188.43×10^3 [a]
H_v	Water vapour enthalpy (J kg^{-1})	2582.4×10^3 [a]
μ	Water molar mass (kg mol^{-1})	18.0153×10^{-3} [a]

[a]From NIST Chemistry WebBook at 5 MPa and 45 °C, [b] Chiquet *et al.* (2007), [c] Sander (2015) and [d] Cadogan *et al.* (2014).

Table 2. Physical properties of the samples.

Symbol	Property	BSP4	DoS-A
K_s	Bulk modulus of the solid matrix (GPa)	30[a]	47[b]
ϕ	Porosity (per cent)	19.6	26.4
k	Permeability (mD)	270	1270
K_d	Bulk modulus of the drained frame (GPa)	12.2	7.1
G_d	Shear modulus of the drained frame (GPa)	11.9	6
l	Sample length (mm)	83.5	82.7
d	Sample diameter (mm)	40.0	38.3

[a]Tarokh & Makhenko (2019), [b] see the Appendix.

(Antioch, CA, USA) and a Berea sandstone sample, purchased from Cleveland Quarries (Vermillion, OH, USA). The Domengine sandstone was chosen because this formation is considered a potential target for large scale geological storage of CO_2. Samples from the Black Diamond Mine Regional Park are composed primarily of quartz (73.8 per cent) and K-feldspar (22.7 per cent) and smaller amounts of smectite (3.5per cent, Voltolini *et al.* 2017). The sample, DoS-A, is coarse grained, with a permeability of 1266 ± 55 mD (at 10 MPa effective pressure) and an average porosity of 26.4 per cent (from X-ray CT). The voxel and slice averaged porosity show some heterogeneity and layering subperpendicular to the x-axis (Fig. 2a). The Berea sandstone was chosen because it is widely used and, consequently, it is well characterized by previous studies. The sample, BSP4, was previously studied by Chapman *et al.* (2021) and furthermore was cored from the same block of Berea sandstone as the sample studied by Chapman *et al.* (2019). The frequency dependent properties and the likely attenuation mechanisms of this sample are therefore well understood and documented. The dominant mineral in Berea sandstones from Cleveland Quarries is quartz (80–95 per cent), with smaller amounts of feldspar and various clays (3–8 per cent, Kareem *et al.* 2017). Sample BSP4 has a permeability of 271 ± 3.5 mD (at 10 MPa effective pressure) and an average porosity of 19.6 per cent (from X-ray CT), with some faint layering visible along the length of the sample (Fig. 2b). Table 2 summarizes the samples physical properties.

Both samples had their end surfaces machined parallel to each other with a diamond-studded grinder. For the forced oscillation measurements four strain-gauge pairs were attached at 90° intervals and centred on the lateral surfaces. Before attaching the strain-gauges, small patches on samples surfaces were prepared with a thin layer of resin that was subsequently ground down to the grains. The strain-gauges and connecting wires were covered with a thin layer of soft epoxy, to prevent corrosion. The samples were then placed in a rubber jacket with an additional outer layer of either aluminium or copper foil to minimize the diffusion of CO_2 from the sample into the confining medium. Before mounting the samples in the experimental set-ups, they were dried in an oven at 60–70 °C.

3.4 Experimental procedure

The operating fluids in our experiments were CO_2 and deionized (DI) water. In a mixing vessel the CO_2 was brought into contact with the DI water at a pressure of either 5 or 10 MPa, respectively, referred to hereafter as the low- and high-pressure experiments. The CO_2 and water were mixed for at least 24 hr to ensure that equilibrium was reached between the two fluids. A Quizix pump was used to circulate the water, by drawing water from the bottom and re-injecting it into the top of the mixing vessel. The temperature in the vessel was regulated at 45 °C with an external heating element. Additional details on the experimental set-up and procedure can be found in Chapman *et al.* (2021).

Before injecting the CO_2 saturated water, air was first removed from the dry samples with a vacuum pump and then the samples were flushed with CO_2 gas. Multiple pore volumes of DI water were subsequently injected into the samples and the pore pressure raised to 6 MPa to dissolve the residual CO_2. The CO_2 saturated water was then transferred from the mixing vessel to the samples at a maximum flow rate of 5 ml min^{-1}, with a back pressure pump maintaining the pore pressure above 5 and 15 MPa, for the respective experiments. To ensure that the DI water is completely replaced, at least 5 pore volumes of CO_2 saturated water were flushed through the samples.

Partial saturation, that is the presence of both CO_2 and water, in the pore space of the samples was achieved by reducing the pore fluid pressure below the equilibrium pressure, which induced the exsolution of CO_2 from the water. To reduce the pore pressure, the confining pressure was hydrostatically reduced under undrained conditions, allowing the pore volume to increase and the pore pressure to decrease (Skempton 1954; Crews & Cooper 2014). Undrained conditions were achieved by closing the micro-valves in the sample holders. For the low pressure experiments the initial pore pressure was set to ∼5.5 MPa. The confining pressure was then reduced from 19 to 15 MPa. For each sample (Berea and Domengine), two low pressure experiments were performed, with the only difference being that the confining pressure was reduced at a rate of 6.5 and 0.02 MPa min^{-1}. A single experiment was performed on sample DoS-A where the exsolved CO_2 was supercritical. In this case the initial pore pressure was 13 MPa and the confining pressure was reduced from 26.5 to 20 MPa, at a rate of 6.5 MPa min^{-1}. From the volumetric strain measured during the depressurization we infer a CO_2 saturation of ∼0.1 per cent for sample BSP4 and ∼0.1 to ∼0.2 per cent for sample DoS-A (appendix B of Chapman *et al.* 2021). The inferred saturation is in good agreement with direct measurements of the pore-volume change, measured with the Quizix pump, of the water saturated sample DoS-A for the same change in effective pressure.

Forced oscillations were performed on the samples 3–4 hr after initiating the reduction in the confining pressure. This time is given to allow the pore pressure to equilibrate in response to the exsolution of CO_2. The pore pressure could not be directly measured

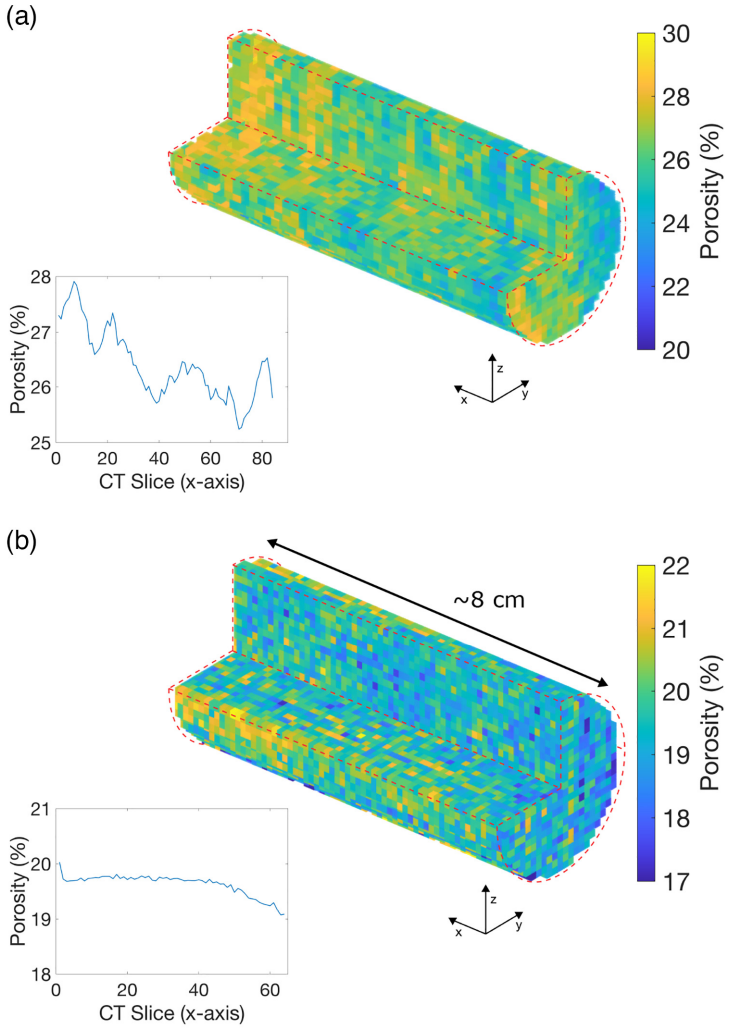

Figure 2. 3-D porosity distribution and slice averaged porosity for samples (a) DoS-A and (b) BSP4 (adapted from Chapman *et al*. 2021). The porosity is reconstructed from the dry and water saturated medical X-ray computed tomography scans taken along the *x*-axis. The voxel dimensions are (1.5 × 1.5 × 2) mm^3 and (1.5 × 1.5 × 1.25) mm^3 for DoS-A and BSP4, respectively.

during experiments because the microvalves in the sample holder are closed. The final pore pressure was therefore inferred at the end of the experiments from the response of the strain gauges when the micro valves were opened again. For the low-pressure experiments, the pore pressure was generally on the order of ∼5 MPa, while for the high-pressure experiment the pore pressure was ∼9 MPa (CO_2 is supercritical). The effective pressure during measurements was ∼10 MPa for the low-pressure experiments and ∼11 MPa for the high-pressure experiment. After the completion of an experiment the pore pressure was raised above the equilibrium pressure to redissolve the CO_2 in the water.

Two exsolution experiments were performed on sample DoS-A under X-ray CT to investigate the fluid saturation distribution. These experiments were performed at slightly lower pressure and temperature conditions. Exsolution of CO_2 was induced by regulating the fluid pressure with a back pressure pump by imposing a pressure decline rate of ∼4.3 MPa and 0.002 MPa min^{-1}. Scans of the sample were taken after exsolution, at a fluid pressure of 3.4 MPa and a temperature of 30 °C. The effective pressure on the sample was 10 MPa. As with the forced oscillation measurements the X-ray CT scans of the partially saturated samples were performed after the pore pressure had equilibrated. A summary of all experiments performed in this study is presented in Table 3.

4 EXPERIMENTAL RESULTS

4.1 Preliminary measurements

Preliminary measurements were performed on both samples before conducting the CO_2 exsolution experiments. First, the dry samples were subjected to three hydrostatic confining pressure loading cycles to assess the mechanical isotropy of the samples. For sample BSP4 the confining pressure was increased from 3 to 20 MPa and for sample DoS-A it was increased from 5 to 15 MPa. During the cycling, sample BSP4 exhibited a difference between the axial and radial strains of between 3 and 6 per cent, while sample DoS-A exhibited a difference of ∼1 per cent. In addition, forced oscillation measurements were performed on the fully water saturated samples under drained and undrained conditions at 45 °C. Drained conditions were achieved by connecting two syringe pumps, filled with a total of 400 ml of water, to the samples. The inferred drained bulk and

Table 3. Overview of experiments.

Measurement	Sample	Experiment ID	Initial P_c (MPa)	Final P_c (MPa)	Initial P_p (MPa)	Final P_p (MPa)	ΔP (MPa min^{-1})	CO_2 saturation (per cent)	Mode of ΔP
Medical X-ray CT	DoS-A	Exs-7	13.4	13.4	5.3	3.4	4.3	0.3	Back pressure
	DoS-A	dP3	13.4	13.4	5.3	3.4	0.002	0.6	Back pressure
Forced oscillation	BSP4	Exs-5	19	15	5.5	~5[a]	6.5	0.1	Hydrostatic
	BSP4	Exs-6	19	15	5.5	~5[a]	0.02	0.1	Hydrostatic
	DoS-A	Exs-1	19	15	5.5	~5.2[a]	6.5	0.2	Hydrostatic
	DoS-A	Exs-2	19	15	5.5	~4.6[a]	0.02	0.2	Hydrostatic
	DoS-A	Exs-2b scCO_2	26.5	20	13	~9[a]	6.5	0.1	Hydrostatic

[a]Inferred after opening microvalves following completion of the experiment.

shear moduli of the samples listed in Table 2 are the average of measurements performed at <10 Hz, because the drained-to-undrained transition occurs at between 20 and 50 Hz. The following section will present the results of the forced oscillation measurements performed on the partially saturated samples and the CO_2 distribution observed in sample DoS-A with the X-ray CT.

4.2 Forced oscillation measurements in partially saturated conditions

4.2.1 Low pore pressure experiments

Fig. 3 shows the measured Young's modulus and Poisson's ratio and the corresponding attenuation with respect to frequency in sample BSP4. In both experiments (Exs-5 and Exs-6), the partially saturated sample exhibits dispersion in the Young's modulus (Fig. 3a) and Poisson's ratio (Fig. 3b). At low frequencies the Young's modulus of the partially saturated sample is on the order of the Young's modulus measured in the fully water saturated drained sample (solid red line, E_{drained} ~27 GPa). In contrast the Poisson's ratio in the partially saturated sample at low frequencies is elevated with respect to Poisson's ratio in the fully water saturated drained sample (red solid line, $\nu_{\text{drained}} \sim 0.13$). The attenuation in the partially saturated sample is frequency dependent with a maximum at ~100 Hz (Fig. 3c). The attenuation associated with the Poisson's ratio exhibits large errors (Fig. 3d), which may be related to the failure of one of the radial strain gauges during the experiments. Overall, there is no discernible difference between experiments Exs-5 and Exs-6. Included in Fig. 3 are also the results of the measurement performed on the fully water saturated sample with undrained boundary conditions. Under these conditions the sample is, as expected, significantly stiffer and the attenuation is low and frequency independent.

Fig. 4 shows the measured Young's modulus and Poisson's ratio and the corresponding attenuation with respect to frequency in sample DoS-A. The partially saturated sample (Exs-1 and Exs-2) exhibits significant dispersion in both the Young's modulus (Fig. 4a) and Poisson's ratio (Fig. 4b). At low frequencies the Young's modulus of the partially saturated sample is again on the order of the Young's modulus measured in the fully water saturated drained sample (solid red line, E_{drained} ~14 GPa). The Poisson's ratio in the partially saturated sample at low frequencies is significantly elevated with respect to Poisson's ratio of the fully water saturated drained sample (solid red line, ν_{drained} ~0.17). The attenuation in the Young's modulus is frequency dependent with a maximum at ~100 Hz (Fig. 4c). The attenuation in the Poisson's ratio is also frequency dependent, in experiment Exs-1 the maximum is at ~100 Hz while in Exs-2 the maximum is at >300 Hz (Fig. 4d). The fully water saturated and undrained sample is significantly stiffer with a Young's modulus of ~16 MPa and a Poisson's ratio of 0.35. The corresponding attenuation is small and frequency independent. The pore pressure measured after the forced oscillations, when the micro-valves were opened again, indicated that the pore pressure during Exs-1 was ~5.2 MPa, while for Exs-2 the pore pressure was ~4.6 MPa. The effective pressure between the experiments was therefore not exactly 10 MPa.

4.2.2 High pore pressure experiment

The measured Young's modulus and Poisson's ratio and the corresponding attenuation from experiment Exs-2b following the exsolution of supercritical CO_2 is shown in Fig. 5. Again, the partially saturated sample exhibits dispersion in the Young's modulus and Poisson's ratio (Figs 5a and b). At low frequencies however, the Young's modulus is lower than that measured on the fully water saturated and drained sample (red line). The Poisson's ratio is comparable to that measured in the low pressure experiments (Exs-1 and Exs-2, Fig. 4b). The corresponding attenuation is frequency dependent with a maximum at ~100 Hz (Figs 5c and d). The fully water saturated and undrained sample exhibits a significantly higher Young's modulus and Poisson's ratio and a low attenuation which is frequency independent.

4.3 Fluid distribution

Fig. 6 shows the 3-D and slice averaged (along sample length) CO_2 saturation, reconstructed from the X-ray CT, in sample DoS-A following pressure decline rates of ~4.3 MPa (Fig. 5a) and 0.002 MPa min^{-1} (Fig. 5b). The mean CO_2 saturation of between 0.3 and 0.6 per cent is slightly elevated when compared to the experiments conducted using the hydrostatic depressurization. In both experiments the CO_2 distribution is approximately homogenous with respect to the length of the sample, as seen in the slice averaged CO_2 saturation. The 3-D distribution demonstrates the small scale of the CO_2 heterogeneities, with the slow pressure decline rate showing slightly larger clusters of gas.

5 ANALYSIS AND INTERPRETATION

5.1 Bulk and shear deformation modes

Assuming that the samples are elastic and isotropic, the Poisson ratio and Young's modulus can be used to infer the bulk and shear moduli (e.g. Jaeger *et al*. 2007). Figs 7 and 8 show the frequency dependent bulk and shear moduli with the corresponding attenuation inferred from the axial forced oscillation measurements for the low pressure

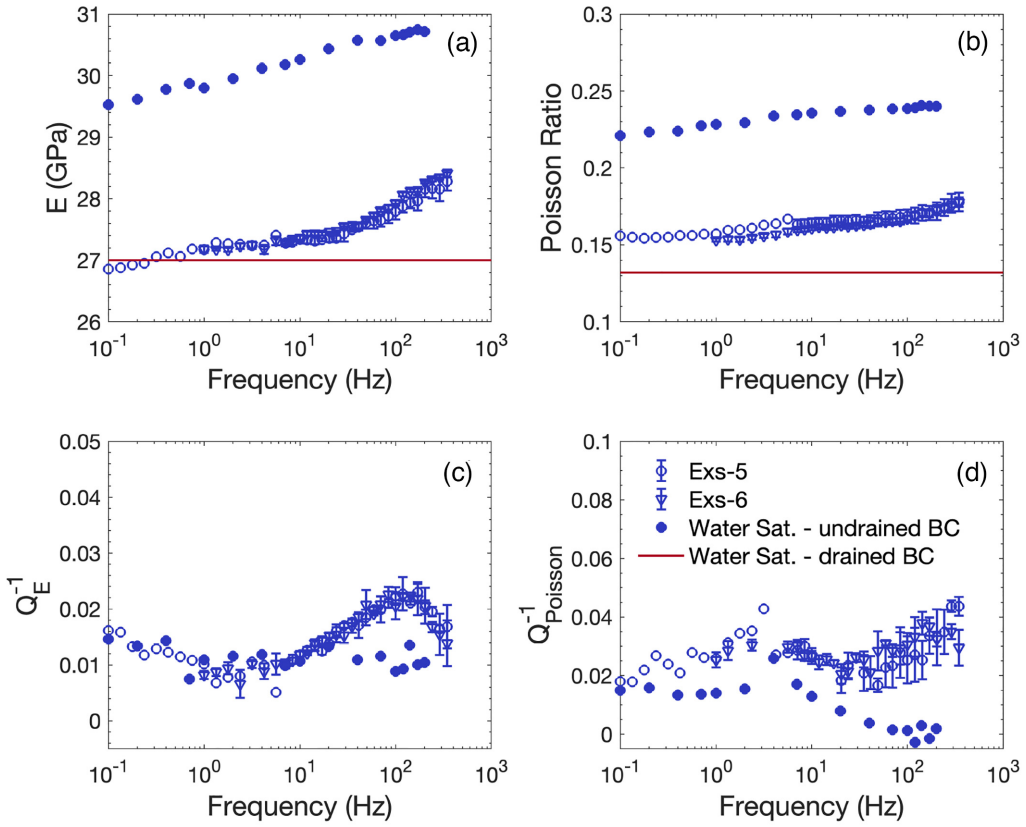

Figure 3. (a) Young's modulus E and (b) Poisson's ratio and the corresponding attenuation (c) Q_E^{-1} and (d) Q_{Poisson}^{-1}, measured on sample BSP4. During experiments Exs-5 and Exs-6 the pore pressure was ∼5 MPa and a CO_2 saturation of 0.1 per cent. The measurements on the fully water saturated sample were performed at a pore pressure of 6 MPa. All measurements were performed at an effective pressure of ∼10 MPa and at 45 °C. The average Young's modulus and Poisson's ratio of the water saturated sample in the drained regime is indicated by the red line. Error-bars correspond to the range around the median of three repeated measurements. Where only a single measurement was performed no error-bars are given.

experiments on samples BSP4 and DoS-A, respectively. Included in both figures are the results of Gassmann's (1951) fluid substitution (eq. 1), utilizing the thermodynamically relaxed fluid bulk modulus (eq. 5) and the unrelaxed fluid bulk modulus (eq. 3), which we refer to as the GLL limit and the GW limit, respectively. For the GW limit we show the results in which we utilize the isothermal and adiabatic CO_2 bulk modulus. The adiabatic fluid bulk modulus K_S is related to the isothermal fluid bulk modulus K_T as:

$$K_S = \gamma K_T, \tag{11}$$

Where γ is the ratio of heat capacity at constant pressure C_p to heat capacity at constant volume C_v (Batzle & Wang 1992). For an ideal gas the isothermal bulk modulus is given by the pressure in the gas. Properties of the fluids are given in Table 1 and the drained bulk and shear moduli used are given in Table 2.

Both partially saturated samples exhibit dispersion with respect to frequency in the bulk (Figs 7a and 8a) and shear modulus (Figs 7b and 8b). In sample BSP4 the bulk modulus lies between the GLL limit at low frequencies and the GW limit at high frequencies. However, for sample DoS-A, while the measured bulk modulus still lies between these limits at low frequencies, it is significantly elevated with respect to the GLL limit. Both partially saturated samples have a reduced shear modulus compared to the corresponding fully water saturated undrained samples. The partially saturated samples also exhibit significant frequency dependent attenuation in both the bulk (Figs 7c and 8c) and shear moduli (Figs 7d and 8d). The overall trend in the attenuation is $Q_K^{-1} > Q_E^{-1} > Q_g^{-1}$. The attenuation in the fully water saturated undrained sample is small and frequency independent. It is important to point out that the shear weakening in the partially saturated samples was reversed when the pore pressure was increased and the sample was again fully water saturated.

The dispersion observed in the bulk modulus in the partially saturated samples (Figs 7a and 8a) is broadly consistent with both a transition from a thermodynamically relaxed to unrelaxed state of the fluids, as described in Section 2, and a transition from drained to undrained conditions (Pimienta *et al*. 2016). For both processes the bulk modulus of the partially saturated sample converges to the GW limit at high frequencies. The microvalves in the sample holders allow for conducting experiments under effectively undrained conditions, as demonstrated by the negligible attenuation and elevated Young's and bulk moduli observed in the fully water saturated samples. However, a small dead volume (30 µl) still exists between the valves and the sample, which could result in a partially drained boundary condition because the presence of a compressible gas will increase the storage capacity of the dead volume (Pimienta *et al*. 2016). This is maybe one explanation for why the measured bulk modulus at low frequencies does not in fact converge to the GLL, as expected when the fluids are thermodynamically relaxed.

Fig. 9 shows the bulk and shear moduli measured on sample DoS-A during the high-pressure experiment. In addition, we have included the results of the bulk modulus (Fig. 9a) and attenuation (Fig. 9c) measured from hydrostatic oscillations at frequencies below 0.1 Hz (symbols in the grey zones). Overall, the observations are in line with those from the low-pressure experiments. For the

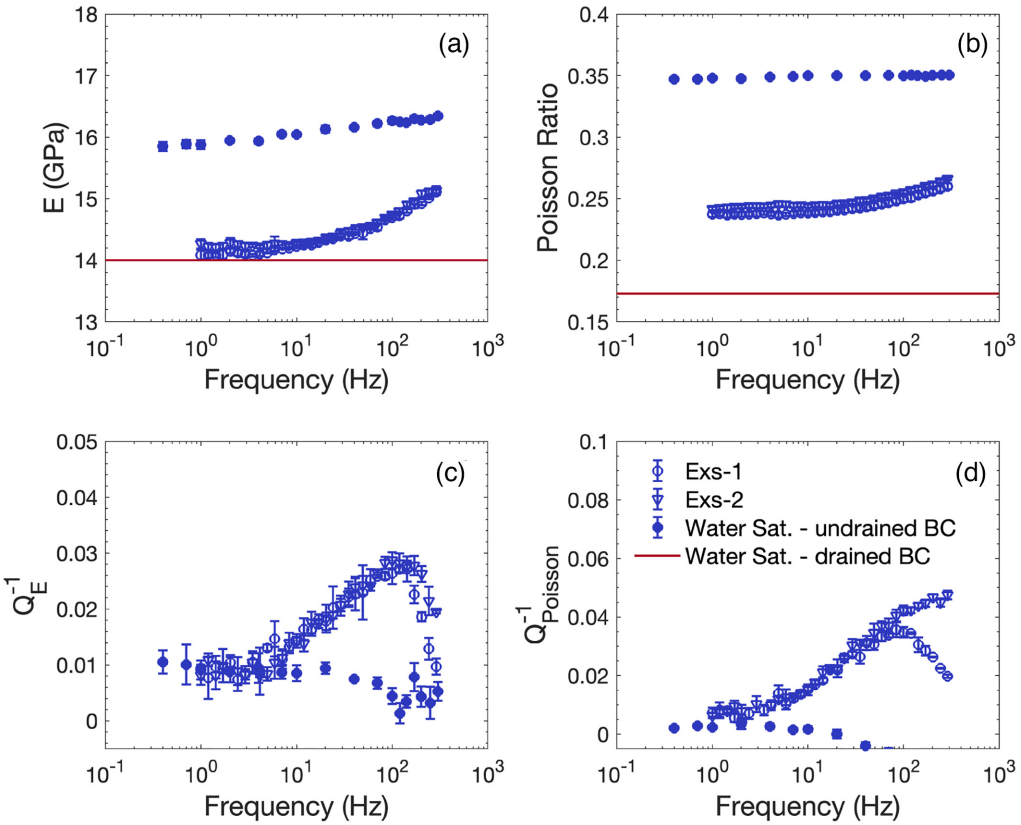

Figure 4. (a) Young's modulus E and (b) Poisson's ratio and the corresponding attenuation (c) Q_E^{-1} and (d) Q_{Poisson}^{-1}, measured on sample DoS-A. During experiments Exs-1 and Exs-2 the pore pressure was 5.2 and 4.6 MPa, respectively, and a CO_2 saturation of 0.2 per cent. The measurements on the fully water saturated sample were performed at a pore pressure of 7 MPa. All measurements were performed at an effective pressure of ∼10 MPa and at 45 °C. The average Young's modulus of the water saturated sample in the drained regime is indicated by the red line. Error-bars correspond to the range around the median of three repeated measurements.

sample partially saturated with supercritical CO_2 the bulk modulus inferred from the axial oscillations lies between the GLL and GW limits. The inferred shear modulus is again frequency dependent and reduced compared to that measured in the fully water saturated sample (Fig. 9b). The maximum attenuation is again observed at ∼100 Hz (Figs 9c and d), however at <5 Hz the attenuation in bulk modulus appears to increase again. The bulk modulus from the hydrostatic oscillations on the fully water saturated drained sample as well as on the partially saturated sample are elevated compared to that inferred from the axial oscillations. In contrast the bulk modulus measured on the fully water saturated undrained sample is reduced with respect to the bulk modulus inferred from the axial oscillations. This discrepancy may be explained by the application of a static axial stress for the axial oscillations, resulting in minor stress induced anisotropy. The attenuation measured during the hydrostatic oscillations (Fig. 9c) suggests another attenuation peak at <0.01 Hz.

As explained in Section 2, Gassmann (1951) predicts that the shear modulus of an isotropic porous material will not be impacted by the saturating fluid (eq. 2). However, as seen in Figs 7(b), 8(b) and 9(b) we observe shear weakening and dispersion in the partially saturated samples. Shear weakening has been widely observed in response to the introduction of water into porous rocks. Even small amounts of water can reduce the measured shear modulus (e.g. Clark *et al*. 1980; Murphy 1984; Murphy *et al*. 1984; Pimienta *et al*. 2014). The reduction in shear modulus can arise from different mechanisms: changes in the surface energy resulting from reactions between the fluids and the porous material (Murphy *et al*. 1984; Pimienta *et al*. 2014; Yin *et al*. 2019), changes in the pore structure related to changes in pore pressure, at constant effective pressure, (Christensen & Wang 1985) or interfacial phenomena at the pore-scale (Rozhko 2020). In both samples, BSP4 and DoS-A, shear weakening was observed between the dry and fully water saturated samples. The additional weakening under partially saturated conditions may indicate that changes in the surface energy/interfacial phenomena are playing a role. The homogenous distribution of the CO_2 following exsolution observed with the X-ray CT (Fig. 6) suggests that the interfacial contact area could be very large and therefore possibly lead to shear weakening as suggested by Rozhko (2020).

The shear modulus dispersion at these low frequencies was not observed by previous studies on partially saturated sandstones (e.g. Spencer & Shine 2016; Chapman *et al*. 2021). The shear modulus dispersion may be explained by both anisotropy and heterogeneity in the solid porous material (e.g. Mavko & Jizba 1991; Berryman & Wang 2001; Berryman 2004; Quintal *et al*. 2012). At the pore scale, such heterogeneity can result in frequency dependent attenuation and dispersion in the shear modulus and is associated with fluid pressure diffusion between compliant cracks or grain contacts and stiff isometric pores, also referred to as squirt flow (e.g. O'Connell & Budiansky 1977; Mavko & Jizba 1991; Chapman *et al*. 2002; Gurevich *et al*. 2010). However, dispersion and attenuation in response to squirt flow is typically not observed in the seismic frequency range (<1000 Hz) unless the saturating fluid has a very

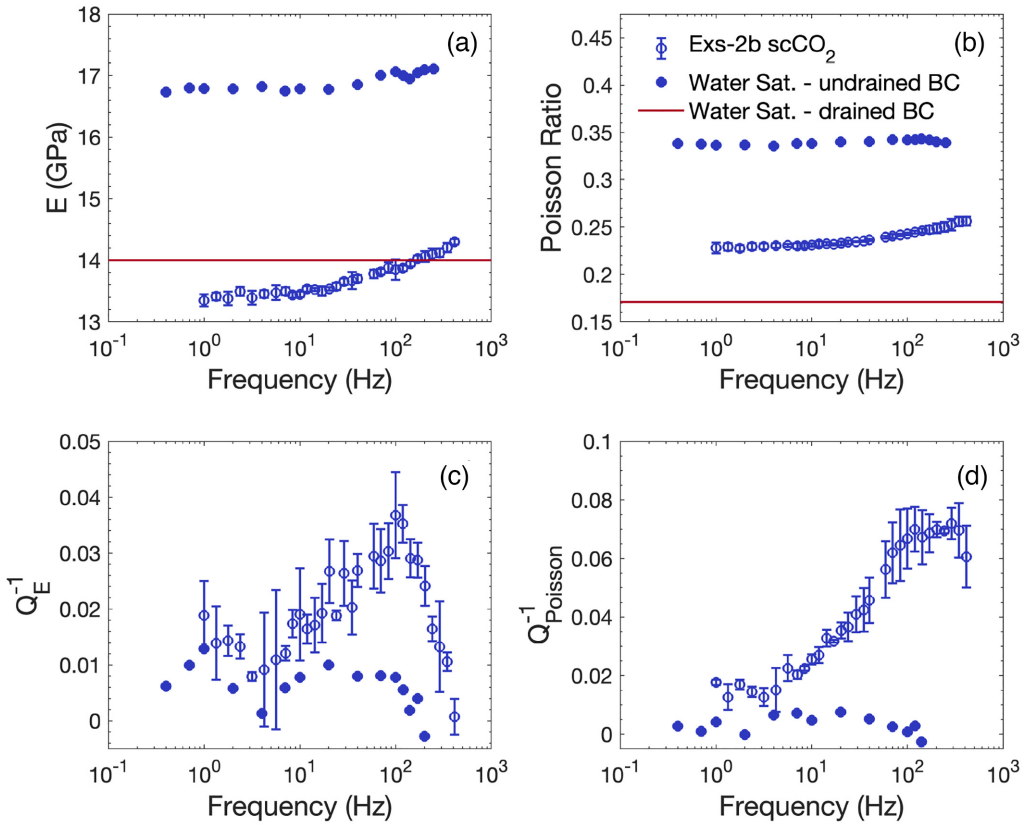

Figure 5. (a) Young's modulus E and (b) Poisson's ratio and the corresponding attenuation (c) Q_E^{-1} and (d) Q_{Poisson}^{-1}, measured on sample DoS-A. During experiment Exs-2b $scCO_2$ the pore pressure was 9 MPa and CO_2 saturation was 0.1 per cent. The measurements on the fully water saturated sample were performed at a pore pressure of 10 MPa. All measurements were performed at an effective pressure of ∼11 MPa and 45 °C. The average Young's modulus of the sample in the drained regime is indicated by the red line. Error-bars correspond to the range around the median of three repeated measurements. Where only a single measurement was performed no error-bars are given.

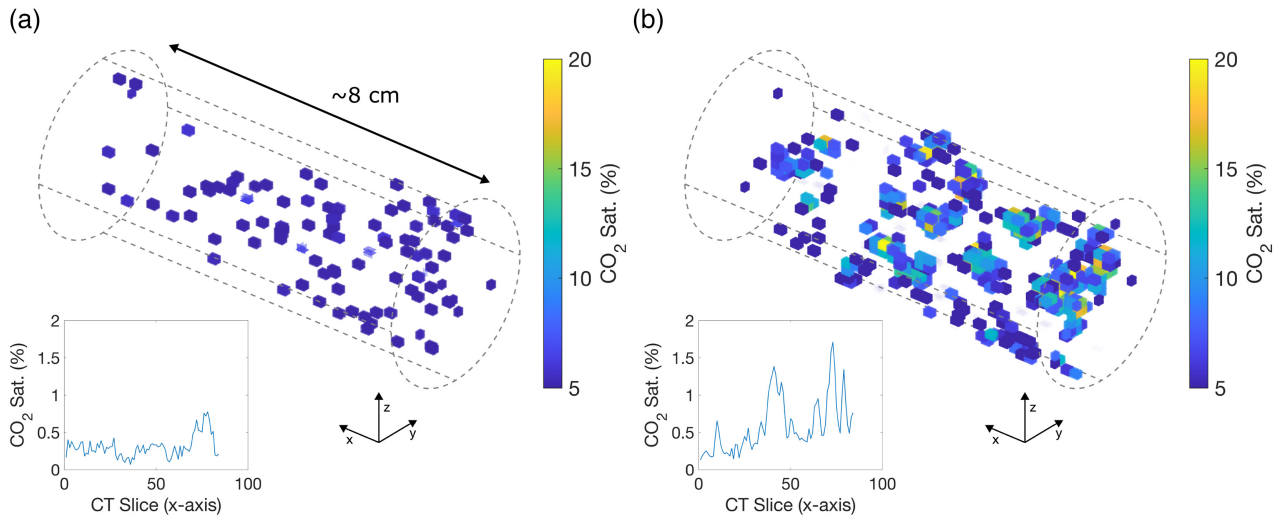

Figure 6. 3-D and slice average CO_2 saturation distribution in sample DoS-A following (a) rapid (∼4.3 MPa min^{-1}) and (b) slow (0.002 MPa min^{-1}) depressurization. Scans were taken approximately 2 and 21 hr after depressurization, for (a) and (b), respectively. The mean saturation is ∼0.3 per cent for (a) and ∼0.6 per cent for (b). The voxel dimensions are (1.5 × 1.5 × 2) mm^3. Saturation values below 4.5 per cent are set to zero and therefore appear transparent. CT Slice 0 corresponds to the outlet side of the sample from which the pore pressure was reduced.

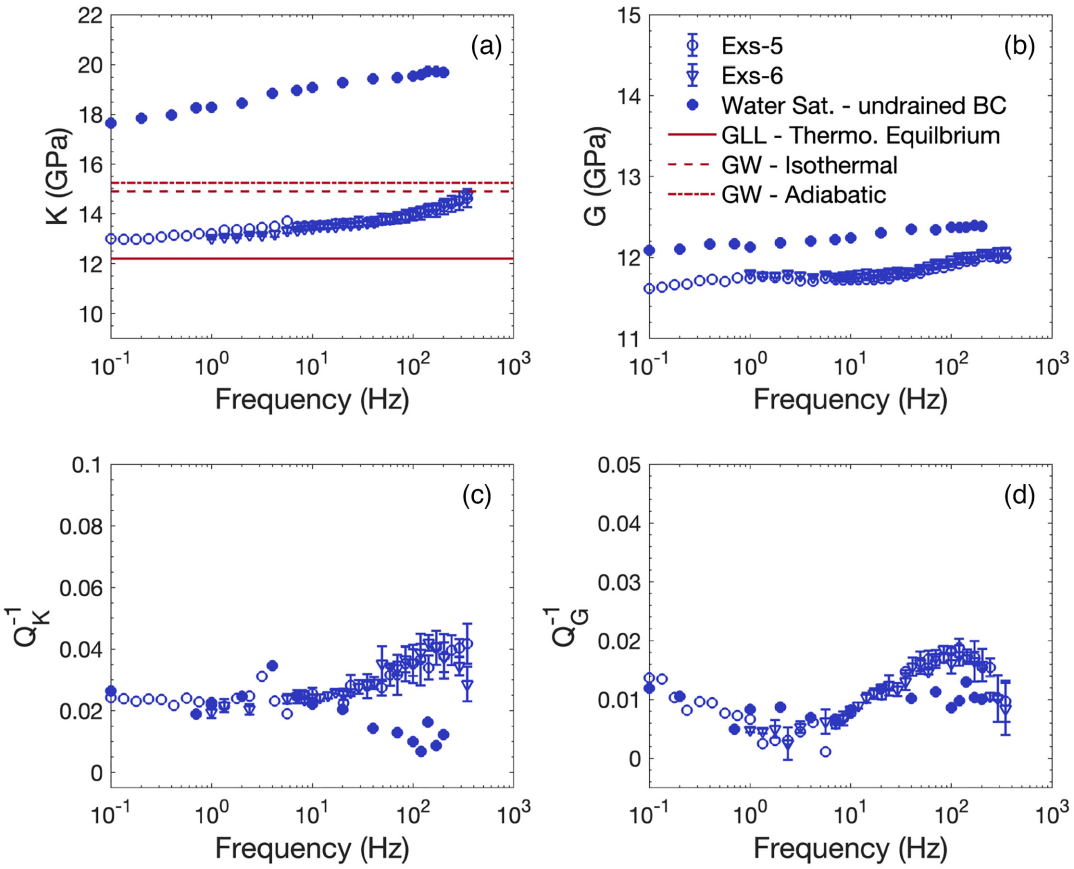

Figure 7. (a) Bulk K and (b) shear G moduli and the corresponding attenuation (c) Q_K^{-1} and (d) Q_g^{-1} inferred for sample BSP4 from experiments Exs-5 and Exs-6. In red are shown the low frequency Gassmann–Landau–Lifshitz (GLL) limit and the high frequency Gassmann–Wood (GW) limit, using the isothermal and adiabatic CO_2 compressibility.

high viscosity. Both Mikhaltsevitch *et al*. (2015) and Chapman *et al*. (2019) conducted forced oscillation measurements on Berea sandstones and observe shear dispersion and attenuation only when the samples were fully saturated with glycerin, a fluid which is three orders of magnitude more viscous than water. Their observations are likely caused by squirt flow. Furthermore, Chapman *et al*. (2019) do not observe dispersion in the shear modulus in response to a transition from drained to undrained conditions.

At the mesoscopic scale, anisotropy and heterogeneity in the porous material can also produce dispersion and attenuation in the shear modulus at seismic frequencies (e.g. Chapman 2003; Masson & Pride 2007). Quintal *et al*. (2012) demonstrated numerically that mesoscopic heterogeneities in the porous material can produce shear attenuation and dispersion in partially saturated conditions. However, Chapman *et al*. (2021) also performed forced oscillation measurements on sample BSP4 following the exsolution of CO_2, at 1 MPa pore pressure and room temperature, and observed no shear dispersion or weakening. In that specific case, based both on a qualitative and quantitative analysis, the dispersion and attenuation in the Young's and bulk moduli were attributed to mesoscopic scale fluid pressure diffusion due to a heterogenous distribution of CO_2. Neither fluid pressure diffusion at the micro or mesoscopic scale appears to therefore be able to adequately explain the shear dispersion and attenuation observed in the partially saturated samples (Figs 7, 8 and 9).

The fact remains that the transition from a thermodynamically relaxed to unrelaxed state of the fluids also does not explain the dispersive shear modulus, unless the samples are locally anisotropic and heterogenous. The preliminary measurements (Section 4.1) on the samples indicated that sample BSP4 does have some degree of anisotropy, while sample DoS-A does not. However, the porosity distribution determined with the X-ray CT shows that sample DoS-A has a degree of heterogeneity (Fig. 2a) at the mesoscopic scale. Meanwhile, both samples can be expected to have significant heterogeneity at the pore scale. Such heterogeneity can result in the local compression of the fluids in response to an external shear boundary condition (Berryman & Wang 2001; Quintal *et al*. 2012) and therefore also lead to a transition from a thermodynamically relaxed to unrelaxed state of the fluids as laid out in Section 2. In the following sections we will investigate: (i) the role of the boundary conditions of our experiments at the mesoscopic scale by conducting simulations of forced oscillations by numerically solving Biot's equations of consolidation in a homogenous medium and (ii) the role of pore scale heterogeneity on the shear modulus by conducting numerical simulations based on the coupled Navier–Stokes and elastic equations.

5.2 Mesoscopic poroelastic numerical simulations

To investigate the role of the remaining dead volume and the presence of gas therein we simulated forced oscillation measurements by numerically solving Biot's (1941) quasistatic equations of poroelastic consolidation in the displacement-pressure formulation (Quintal

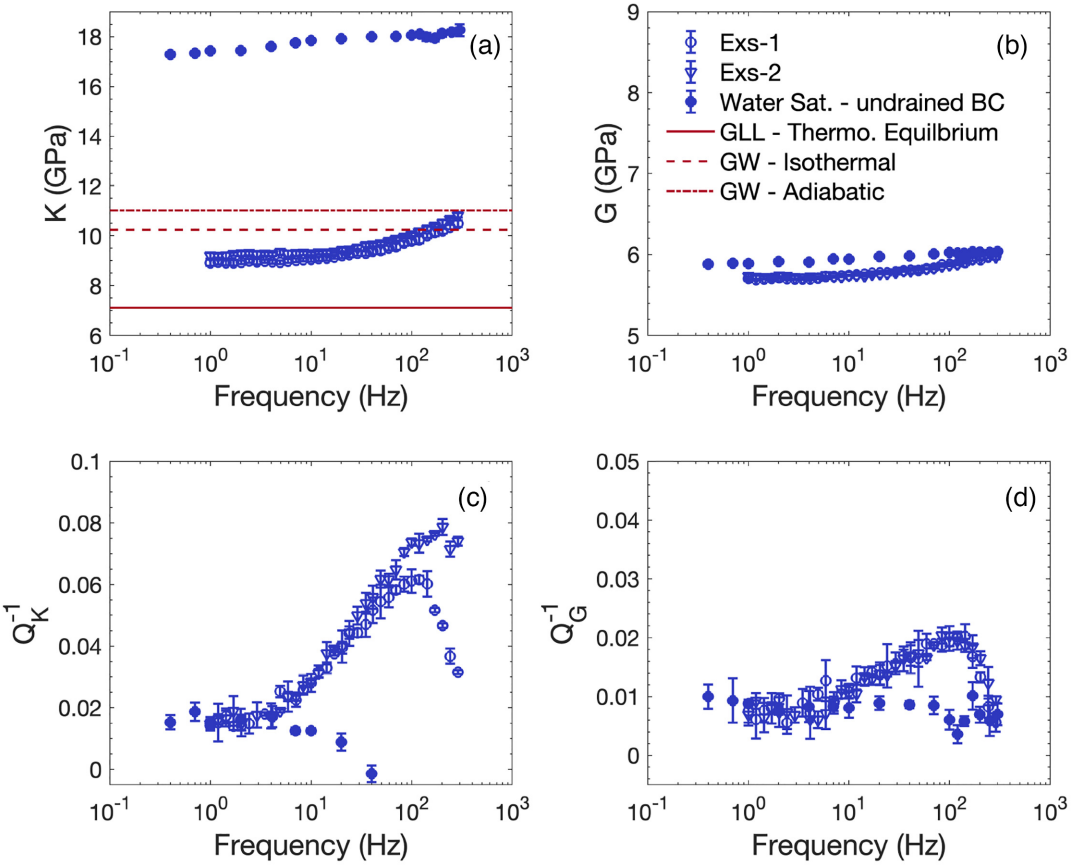

Figure 8. (a) Bulk K and (b) shear G moduli and the corresponding attenuation (c) Q_K^{-1} and (d) Q_g^{-1} inferred for sample DoS-A from experiments Exs-1 and Exs-2. In red are shown the low frequency Gassmann–Landau–Lifshitz (GLL) limit and the high frequency Gassmann–Wood (GW) limit, using the isothermal and adiabatic CO_2 compressibility.

et al. 2011). The equations are solved in COMSOL Multiphysics, utilizing the finite element method, in the same way as previously outlined in Chapman *et al*. (2018) and Chapman *et al*. (2021). We consider a 3-D numerical model composed of a cylinders representing the sample and two smaller cylinders representing the dead volumes (Fig. 10a). The portions of the model representing the dead volumes are given properties of a very stiff ($K_d = 90$ GPa, $G_d = 70$ GPa, $K_s = 108$ GPa), highly porous (99 per cent) and permeable (10 Darcy) isotropic and homogenous material. The portion of the model representing the sample is also homogenous and isotropic, with the properties and dimensions of samples of BSP4 and DoS-A, found in Table 2.

To simulate uniaxial compression tests, a vertical time-harmonic oscillatory displacement is applied to the top boundary of the sample and top of the dead volume, while a zero-displacement boundary condition is applied in the vertical direction on the bottom boundary of the sample and the bottom of the dead volume. The lateral boundaries of the sample are free and can be displaced in the horizontal direction, allowing for the direct determination of the Young's modulus. Both dead volumes are prescribed zero displacement boundary conditions in the horizontal direction on the lateral boundaries. All model boundaries have by default undrained boundary conditions. The frequency-dependent and complex Young's modulus is determined from the vertical stress and strain averaged over the volume of a 6-mm-thick slice at the centre of the sample, to represent the local measurement of strain gauges (Chapman & Quintal 2018). The corresponding attenuation is determined from the ratio between the imaginary and real parts of the complex Young's modulus (O'Connell & Budiansky 1978).

For both samples we investigate (i) the impact of the dead volumes being partially filled with CO_2 and (ii) when the entire model domain is filled by a fluid with a complex fluid bulk modulus arising from the exsolution–dissolution of micrometric CO_2 bubbles. For the first scenario we consider that both dead volumes are half filled with CO_2 and half filled with water, with the gas placed next to the sample. As indicated by the X-ray CT, the CO_2 exsolved likely rather homogeneously throughout the sample (Fig. 6), the sample is therefore assumed to be saturated by an effective single phase fluid where the fluid bulk modulus is real valued and simply determined from a Reuss average (eq. 3) and the fluid viscosity is described according to Teja & Rice (1981) as:

$$\eta_f = \eta_g \left(\frac{\eta_l}{\eta_g} \right)^{S_l}, \tag{12}$$

where η_g and η_l are the viscosity of CO_2 and water, respectively. S_g and S_l are the gas and liquid saturation such that $S_g + S_l = 1$. The total gas saturation in the two models is 0.1 and 0.2 per cent for BSP4 and DoS-A, respectively. However, with half of all the CO_2 placed in the dead volumes, the sample domain of the models only have a gas saturation of ∼0.02 and 0.13 per cent for BSP4 and DoS-A, respectively.

For the second scenario we first solved for the complex fluid bulk modulus resulting from the dissolution–exsolution of a gas bubble as outlined in Section 2.2. We considered a gas bubble with a radius

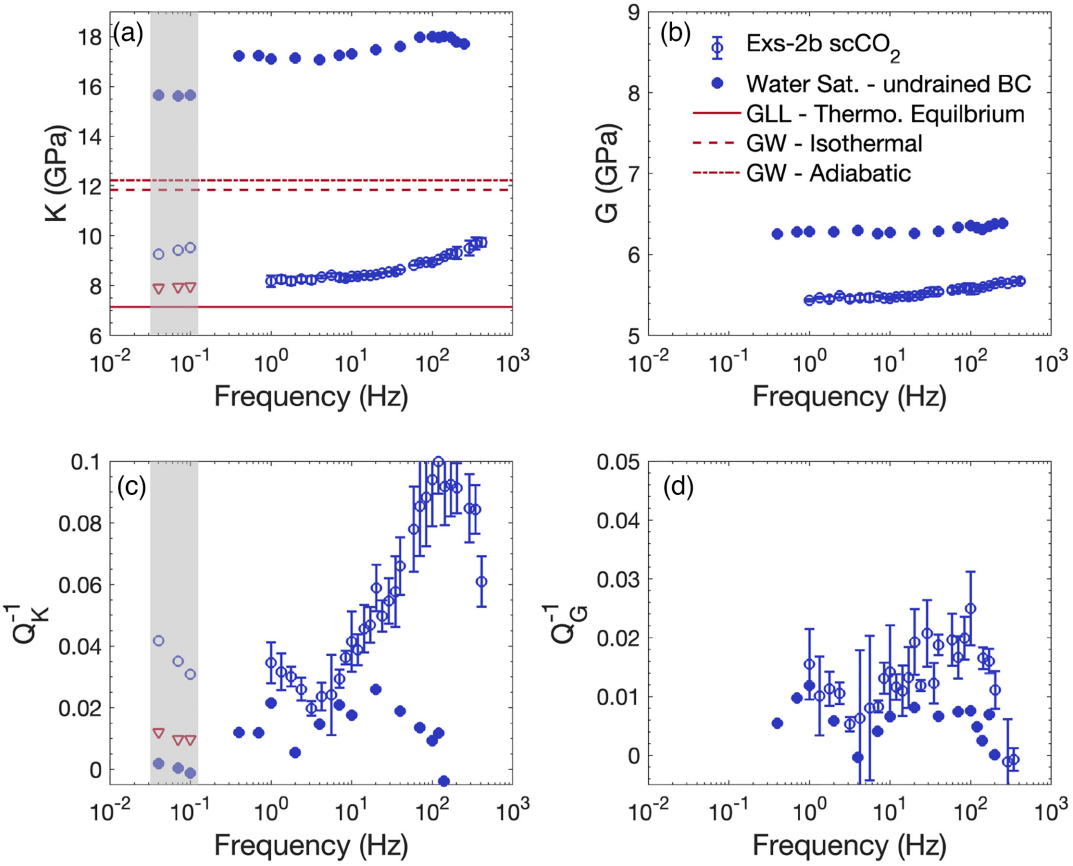

Figure 9. (a) Bulk K and (b) shear G moduli and the corresponding attenuation (c) Q_K^{-1} and (d) Q_g^{-1} inferred for sample DoS-A from experiment Exs-2 $scCO_2$. The data points in the grey shaded zone correspond to the bulk modulus and attenuation measured from hydrostatic oscillations of the confining pressure. The inverted red triangles are the measurements from the fully water saturated sample with drained boundary conditions. The red lines are the low frequency Gassmann–Landau–Lifshitz (GLL) limit and the high frequency Gassmann–Wood (GW) limit, using the isothermal and adiabatic CO_2 compressibility and the drained bulk modulus determined from the axial oscillations.

of 2 μm, at a pressure of 5 MPa and 45 °C and a gas saturation of 0.13 and 0.2 per cent for BSP4 and DoS-A, respectively. The complex and frequency dependent fluid bulk modulus is imported into COMSOL as a function dependent on frequency and is prescribed over the entire model, including the dead volumes. All fluid properties utilized in the simulations are listed in Table 1.

Figs 10(a) and (b) show the results of the different numerical simulations and how they compare to the Young's modulus and attenuation measured in the low pore pressure experiments from samples BSP4 and DoS-A. The presence of a significant amount of gas in the dead volumes has a small impact on the attenuation and dispersion. However, it is not sufficient to explain the laboratory measurements where for both samples, the measured Young's modulus is significantly lower. It should be noted that the amount of gas present in the dead volume during the experiments is unknown. Incorporating the complex and frequency dependent fluid bulk modulus into the models is in closer agreement with the laboratory measurements. However, the attenuation is overestimated in both samples and the laboratory measurements show a slightly broader dispersion in the Young's modulus.

5.3. Micromechanical numerical simulations

We investigate the role of pore-scale heterogeneity and anisotropy with the help of micromechanical simulations in which we numerically solve the coupled quasistatic Lame–Navier and Navier–Stokes equations (Quintal *et al*. 2019). The coupled equations can be used to describe laminar flow of a viscous and compressible fluid surrounded by an isotropic elastic and linear solid background material. Again, we use COMSOL Multiphysics to solve the coupled equations with the finite element method. We consider a 2-D rectangular model of a pore-space embedded in solid grain material. To assess the shear attenuation and modulus dispersion an oscillatory test is performed by applying a horizontal displacement to the top model boundary, while the horizontal and vertical displacements at the bottom boundary are set to zero. The vertical displacements on the side boundaries are also set to zero. Due to the pore-space being fully embedded in grain material the model is undrained. The complex and frequency dependent shear modulus is determined as:

$$G = \frac{1}{2}\frac{\sigma_{xy}}{\epsilon_{xy}}, \tag{13}$$

where σ_{xy} and ϵ_{xy} are the shear stress and strain averaged over the total model domain, respectively. As in Section 5.2, the corresponding attenuation is determined from the ratio between the imaginary and real parts of the complex modulus (O'Connell & Budiansky 1978).

The 2-D model is composed of a pore space consisting of a thin and uniform crack connected to a circular pore, comparable to the conceptual model for squirt flow of Murphy *et al*. (1986) or Gurevich *et al*. (2010), and is embedded in grain material. The

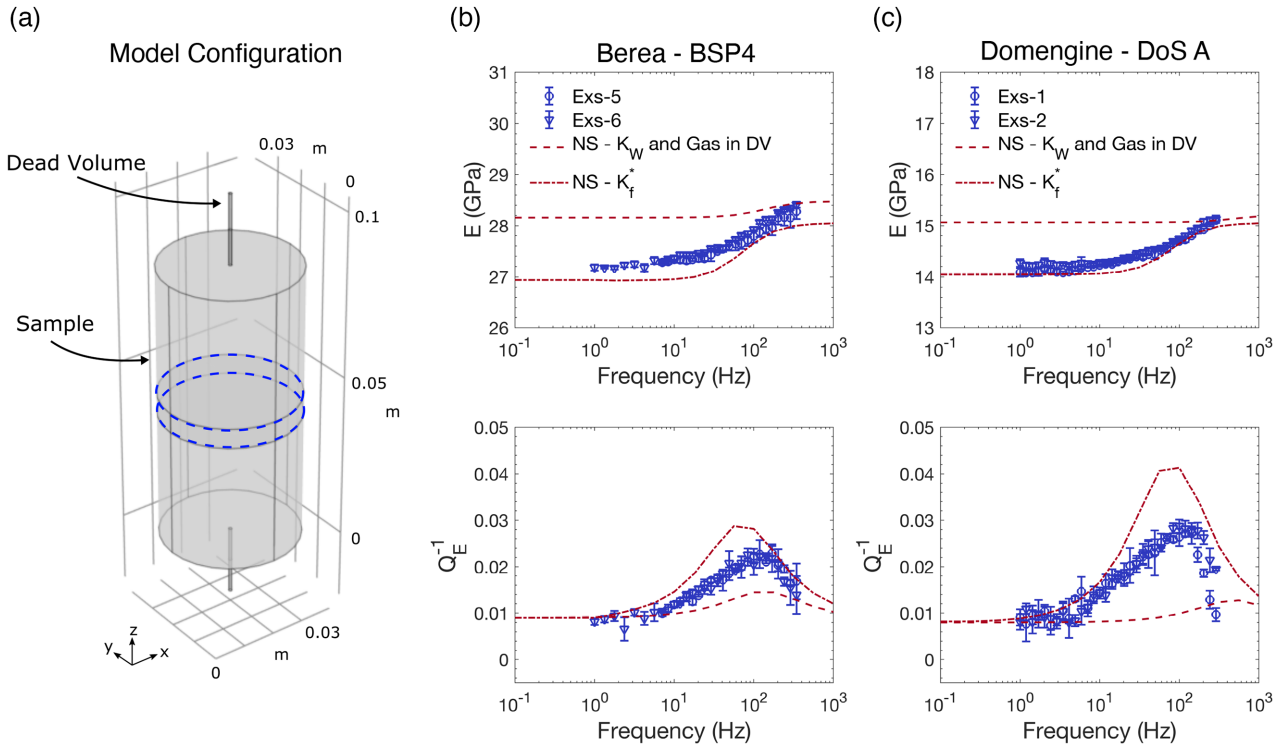

Figure 10. (a) Schematic representation of the 3-D model for the poroelastic numerical simulations. The dead volumes are given properties of a stiff, highly porous and permeable material and have a diameter of 1 mm and a length of 21 mm. The properties and dimensions of the samples are given in Table 2. The dashed blue lines indicate the volume over which we average the stress and strain. Comparison of the poroelastic numerical simulations and measurements of Young's modulus E and attenuation Q_E^{-1} from samples (b) BSP4 and (c) DoS-A, respectively. Laboratory measurements are presented in blue and the numerical simulations are given in red. The numerical simulations consider two scenarios: one where half the dead volume is filled with gas and the rest of the sample is saturated by an effective single-phase fluid (NS – K_w) and another where the entire model is given a complex fluid bulk modulus K_f^* (NS – K_f^*). The complex fluid bulk modulus K_f^* is determined from the exsolution–dissolution model for a bubble with a radius of 2 μm, at a pressure of 5 MPa and 45 °C and a CO_2 gas saturation of 0.13 and 0.2 per cent for BSP4 and DoS-A, respectively.

crack is inclined at 45° to the horizontal plane and has a length of 50 μm and a width of 0.125 μm, giving it an aspect ratio of 0.0025. The circular pore has a radius of 25 μm. The external grain material consists of a square with 100-μm-long sides. The model has a porosity of 0.197 and a crack porosity of 6.25×10^{-4}. The crack aspect ratio and porosity are the same as those used by Chapman *et al*. (2019) in the analytical solution of the Gurevich *et al*. (2010) squirt-flow model to analyse the attenuation and dispersion observed in a glycerin saturated Berea sandstone sample, taken from the same block as sample BSP4. The grain material has properties of quartz, with a bulk modulus of 37 GPa and a shear modulus of 44 GPa. We performed two simulations with this model considering: (i) the fluid having properties of water and (ii) the fluid having the same complex and frequency dependent bulk modulus as in Section 5.2 for one of the poroelastic simulations.

Fig. 11(a) shows the shear modulus dispersion and corresponding attenuation as functions of frequency for the case where the saturating fluid is either water or an effective fluid with a complex and frequency dependent bulk modulus. When the saturating fluid is water, there is only one attenuation peak at ∼30 kHz, which can only be due to fluid pressure diffusion between the compliant crack and stiff pore, know as squirt-flow (e.g. Murphy *et al*. 1986; Gurevich *et al*. 2010). For the case with the effective fluid there are two attenuation peaks, one ∼30 kHz due to squirt flow, as in the case of full water saturation, and another peak at ∼100 Hz. The attenuation peak at ∼100 Hz is a consequence of the complex and frequency dependent fluid bulk modulus. The horizontal displacement leads to a local compression of the pore space that is resisted by the complex fluid, which becomes stiffer with increasing frequency, this is illustrated by the uniform and non-zero fluid pressure of approximately 1 kPa at 100 Hz (Fig. 11b). Fig. 11(b) also shows the fluid pressure at ∼30 kHz, where the fluid pressure inside the crack is approximately an order of magnitude higher than in the stiff pore and it is this pressure difference that results in squirt flow.

The model configuration and dimension (2-D) are of course an oversimplification of the heterogeneity of a real porous rock; however, it illustrates how a shear displacement can produce a local compression (e.g. Berryman & Wang 2001). The increase in pore pressure can therefore perturb the thermodynamic equilibrium between the two fluid phases, as outlined in Section 2. The inclination of the crack at 45° maximizes the pore compression and consequently the attenuation. Though not shown here, we also performed shear displacement simulations on models with cracks symmetrically placed around a circular pore. In these simulations, there was no net change in the pore volume because the compression of a crack was compensated by extension of the opposing crack. With no net change in the pore volume the pore pressure change was zero and there was no shear modulus dispersion or attenuation at 100 Hz.

6 DISCUSSION AND OUTLOOK

The observed attenuation and dispersion could have important implications for seismic monitoring, where the strong sensitivity to

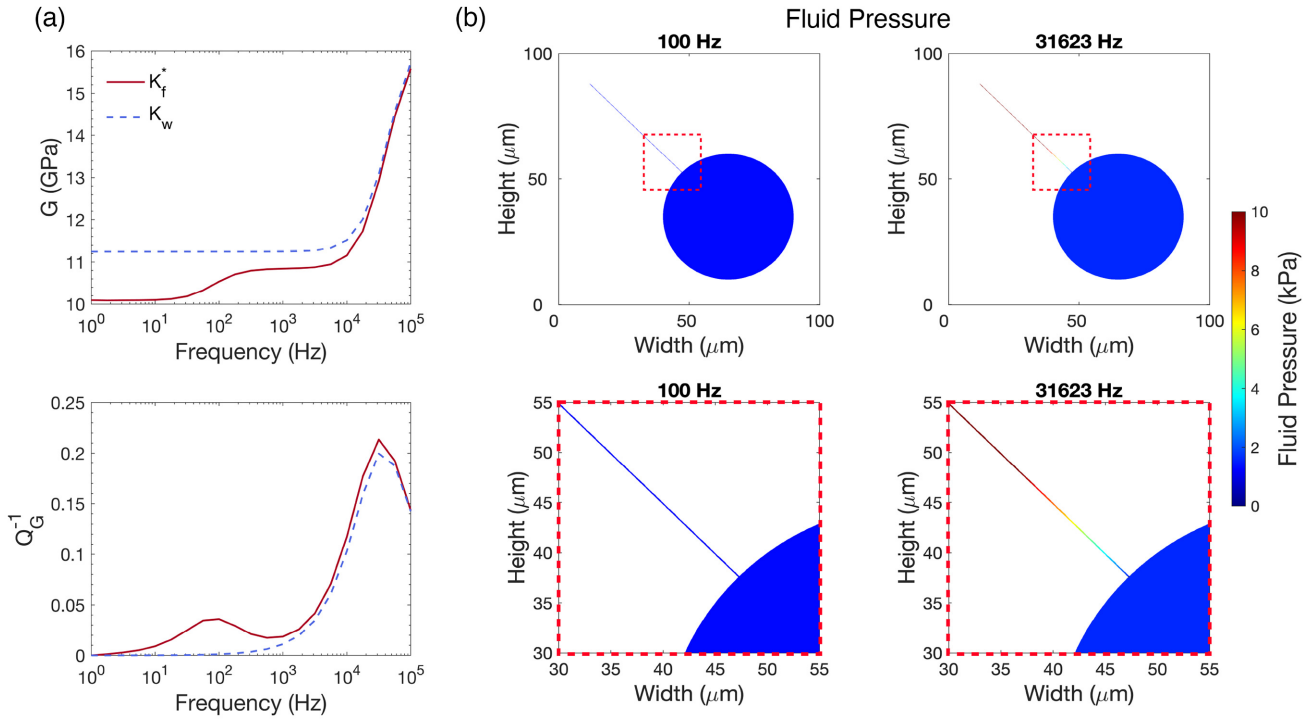

Figure 11. (a) Shear modulus G and the corresponding attenuation Q_g^{-1} determined from micromechanical numerical simulations. Results are shown for when the saturating fluid has a complex fluid bulk modulus K_f^* or a bulk modulus of water K_w, in both cases the fluids have the same viscosity. The complex fluid bulk modulus is determined from the exsolution–dissolution model for a bubble with a radius of 2 μm, at a pressure of 5 MPa, 45 °C and a CO_2 gas saturation of 0.13 per cent. (b) Fluid pressure inside the crack and pore at 100 and 31623 Hz, corresponding to the attenuation peak in response to exsolution–dissolution and squirt-flow, respectively. The red-dashed box outlines the zoom-in on the fluid pressure.

small amounts of gas could be an early sign of reservoir depressurization. For example, at the St Gallen (Switzerland) geothermal site, injection tests in 2013 led to an uncontrolled release of gas and ultimately a M_L 3.5 earthquake. Subsequent analysis of the ambient seismic noise by Obermann *et al*. (2015) showed an aseismic loss of waveform coherence around the injection site 4 days before the release of gas. The loss of waveform coherence was partially attributed to changes in attenuation and reflectivity due to the presence of gas. In another example, Blanchard and Delommot (2015) analysed changes in time-lapse seismic wave attenuation in a reservoir undergoing depletion and found that the gas saturations predicted from a patchy saturation attenuation model exceeded those of PVT (pressure, volume and temperature) and reservoir simulations. The observed shear weakening in our experiments (Figs 7, 8 and 9) also points to physio-chemical interactions of multiphase fluids with the rock which may have important implications for simulations of reservoirs going through large changes in fluid saturation, such as during CO_2 injection (e.g. Krevor *et al*. 2015).

Additional steps are needed to carry our work forward to better understand the impact of heat and mass transfer processes and physiochemical interactions of multiphase fluids on the mechanical properties of porous materials. The model used by Tisato *et al*. (2015), which we also used to determine the effective fluid bulk modulus does not account for heat diffusion or viscous effects and assumes that there is no interaction between the fluid interfaces and the matrix of the rock. The low viscosity of water in our experiments allows for neglecting viscous effects (e.g. Kurzon *et al*. 2015), which are typically taken into account in models for bubbly magmas where the fluid viscosity is between 4 and 9 orders of magnitude more viscous than water (e.g. Lyakhovsky *et al*. 1996; Collier *et al*. 2006). In the context of heavy oil reservoirs, the viscosity should however be considered (e.g. Behura *et al*. 2007). Similarly, assuming little interaction of fluid interfaces with the rock matrix is appropriate for our experiments where the assumed bubble size is smaller than the typical pore size for both Berea and Domengine sandstone (e.g. Madonna *et al*. 2012; Voltolini *et al*. 2017). However, in rocks with smaller pore sizes, significant interaction between the fluid interfaces and the matrix should be expected. To address these aspects, the micromechanical simulations could be extended to solve for heat and mass diffusion in the saturating fluids and allow for investigating the impact of bubble size distribution and interference between nearby bubbles. In 3-D, the approach could be extended to models constructed from synchrotron X-ray CT scans of the samples pore space (Lissa *et al*. 2021). On the experimental side, it would be valuable to conduct experiments over a wider CO_2 saturation range in order to validate that attenuation in response to heat and mass transfer processes is diminished with increasing gas saturation. During such experiments it would be possible to investigate how physiochemical interactions of multiphase fluids impact the differences between dynamic and static moduli of rocks by performing measurements of over a range of the strain amplitudes. This could be beneficial in linking the seismic response of a reservoir to its geomechancial response.

7 CONCLUSIONS

We conducted forced oscillation measurements on two partially saturated sandstone samples to investigate wave attenuation and dispersion at seismic frequencies. Partial gas saturations on the order of 0.1–0.2 per cent CO_2 were achieved by pore pressure

reduction from an initially water saturated state and subsequent exsolution of CO_2. A first set of experiments were performed at a pore pressure of ∼5 MPa, an effective pressure of 10 MPa and 45 °C. Both samples exhibited frequency dependent attenuation and dispersion in the Young's modulus and Poisson's ratio, with an attenuation peak at ∼100 Hz. The measured Young's modulus of the partially saturated samples was, at low frequencies, on the order of the modulus measured in the fully water saturated samples with drained boundary conditions. The bulk and shear modulus, inferred from the Young's modulus and Poisson's ratio, were both dispersive and exhibited frequency dependent attenuation. The bulk modulus was between the GLL limit at low frequencies and the GW limit at high frequencies. These observations point to a transition from a thermodynamically relaxed to unrelaxed state of the fluid mixture saturating the samples. We also observed shear weakening in the partially saturated samples with respect to the water saturated samples. The shear weakening was reversed by redissolving the CO_2 and fully saturating the samples with water. A second set of experiments performed on the Domengine sandstone sample at a pore pressure of ∼9 MPa, an effective pressure of 11 MPa and a temperature of 45 °C corroborated the observations of the low-pressure experiments.

To further investigate these observations, we incorporated an effective fluid bulk modulus, determined from numerical simulations of the dissolution–exsolution of a pore scale gas bubble in water in response to a time harmonic pressure oscillation, into poroelastic and micromechanical numerical models to simulate attenuation and dispersion at the mesoscopic and microscopic scale. Based on the poroelastic simulations we conclude that the remaining dead volume in our experimental setup had no significant impact on our measurements and that the Young's modulus dispersion and attenuation was likely in response to a transition from a thermodynamically relaxed to unrelaxed state. The micromechanical simulations provide support that the observed shear modulus dispersion was possibly a consequence of heterogeneity and or anisotropy in the solid matrix that allow for a local pore compression in response to an external shear boundary condition.

ACKNOWLEDGMENTS

This work was supported by an Early Postdoc.Mobility Fellowship (project no. P2LAP2_181260) from the Swiss National Science Foundation. The experimental work was partially supported by the Region Ile-de-France in the framework of DIM Oxymore, by CNRS via 'Mission pour les Initiatives Transverses et Interdisciplinaires' (MITI) and 'Cellule Energie' of CNRS through the project 'LAB-4D'. The work was also supported by the Global Climate and Energy Project at Stanford University. The authors would like to thank Editor Dr. Andrew Barbour, Yadong Zhang and an anonymous reviewer for their helpful comments. SC would like to thank Maartje Boon, Charlotte Garing and Chris Zahasky for fruitful discussions and support with the experiments using the X-ray CT and data processing. SC would like to also thank Yury Alkhimenkov and Simon Lissa for fruitful discussions and their help with the micromechanical simulations. Special thanks also go to Dr. Timothy Kneafsey for kindly providing the Domengine sandstone sample.

DATA AVAILABILITY STATEMENT

The experimental data are available by contacting the corresponding author (samuel.chapman38@gmail.com).

REFERENCES

Akin, S. & Kovscek, A. R., 2003. Computed tomography in petroleum engineering research, *Geol. Soc. Lond., Spec. Publ.,* **215,** 23–38.

Auriault, J. - L., Boutin, C., Royer, P. & Schmitt, D., 2002. Acoustics of a porous medium saturated by a bubbly fluid undergoing phase change, *Transp. Porous Media,* **46,** 43–76.

Batzle, M. & Wang, Z., 1992. Seismic properties of pore fluids, *Geophysics,* **57,** 1396–1408.

Behura, J., Batzle, M., Hofmann, R. & Dorgan, J., 2007. Heavy oils: their shear story, *Geophysics,* **72**(5), E175–E183.

Berryman, J. B., 1999. Origin of Gassmann's equations, *Geophysics,* **64,** 1627–1629.

Berryman, J. B. & Wang, H. F., 2001. Dispersion in poroelastic systems, *Phys. Rev.,* **64,** doi:10.1103/PhysRevE.64.011303.

Berryman, J. B., 2004. Poroelastic shear modulus dependence on pore-fluid properties arising in a model of thin isotropic layers, *Geophys. J. Int.,* **157,** 415–425.

Biot, M. A., 1941. General theory of three-dimensional consolidation, *J. appl. Phys.,* **12,** 155–164.

Blanchard, T. D. & Delommot, P., 2015. An example of the measurement and practical applications of time-lapse seismic attenuation, *Geophysics,* **80,** WA25–WA34.

Borgomano, J. V. M., Gallagher, A., Sun, C. & Fortin, J., 2020. An apparatus to measure elastic dispersion and attenuation using hydrostatic- and axial-stress oscillations under undrained conditions, *Rev. Scient. Instrum.,* **91,** doi:10.1063/1.5136329.

Cadogan, S. P., Maitland, G. C. & Trusler, J. P. M., 2014. Diffusion coefficients of CO_2 and N_2 in water at temperatures between 298.15 K and 423.15 K at Pressures up to 45 MPa, *J. Chem. Engi. Data,* **59,** 519–525.

Chapman, M., Zatsepin, S. V. & Crampin, S., 2002. Derivation of a microstructure poroelastic model, *Geophys. J. Int.,* **151,** 427–451.

Chapman, M., 2003. Frequency-dependent anisotropy due to meso-scale fractures in the presence of equant porosity, *Geophys. Prospect.,* **51,** 369–379.

Chapman, S., Tisato, N., Quintal, B. & Holliger, K., 2017. Frequency scaling of seismic attenuation in rocks saturated with two fluids phases, *Geophys. J. Int.,* **208,** 221–225.

Chapman, S., Quintal, B., Holliger, K., Baumgartner, L. & Tisato, N., 2018. Laboratory measurements of seismic wave attenuation and Young's modulus dispersion in a partially and fully water-saturated porous sample made of sintered borosilicate glass, *Geophys. Prospect.,* **66,** 1384–1401.

Chapman, S., Borgomano, J. V. M., Yin, H., Fortin, J. & Quintal, B., 2019. Forced oscillation measurements of seismic wave attenuation and stiffness moduli dispersion in glycerine-saturated Berea sandstone, *Geophys. Prospect.,* **67,** 956–968.

Chapman, S., Borgomano, J. V. M., Quintal, B., Benson, S. M. & Fortin, J., 2021. Seismic wave attenuation and dispersion due to partial fluid saturation: direct measurements and numerical simulations based on X-ray CT, *J. geophys. Res.,* **126,** doi:10.1029/2021JB021643.

Chiquet, P., Daridon, J. -L., Broseta, D. & Thibeau, S., 2007. CO_2/water interfacial tensions under pressure and temperature conditions of CO_2 geological storage, *Ener. Conver. Manag.,* **48,** 736–744.

Christensen, N. I. & Wang, H. F., 1985. The influence of pore pressure and confining pressure on dynamic elastic properties of Berea sandstone, *Geophysics,* **50,** 207–213.

Clark, V. A., Tittmann, B. R. & Spencer, T. W., 1980. Effect of volatiles on attenuation (Q-1) and velocity in sedimentary rocks, *J. geophys. Res.,* **85**(B10), 5190–5198.

Crews, J. B. & Cooper, C. A., 2014. Transient pore pressure response to confining stress excursions in Berea sandstone flooded with an aqueous solution of CO2, *Water Resour. Res.,* **50,** 4775–4786.

Collier, L., Neuberg, J. W., Lensky, N., Lyakhovsky, V. & Navon, O., 2006. Attenuation in gas-charged magma, *J. Volc. Geotherm. Res.,* **153,** 21–36.

Coste, C. & Laroche, C., 1993. Acoustic behaviour of a liquid/vapour mixture in a stranding-wave tube, *J. Fluid Mech.,* **246,** 67–89.

Firoozabadi, A. & Pan, H., 2000. Two-phase isentropic compressibility and two-phase sonic velocity for multicomponent-hydrocarbon mixtures, *SPE Reserv. Eval. Eng.,* **3,** 335–341.

Fuster, D. & Montel, F., 2015. Mass transfer effects on linear wave propagation in diluted bubbly liquids, *J. Fluid Mech.,* **779,** 598–621.

Gassmann, F., 1951. Über die Elastizität poröser Medien, *Vierteljahresschr. Naturforsch. Ges. Zürich,* **96,** 1–23.

Grab, M., Quintal, B., Caspari, E., Deuber, C., Maurer, H. & Greenhalgh, S., 2017. The effect of boiling on seismic properties of water-saturated fractured rock, *J. geophys. Res.,* **122,** 9228–9252.

Gurevich, B., Makarynska, D., de Paula, O. B. & Pervukhina, M., 2010. A simple model for squirt-flow dispersion and attenuation in fluid-saturated granular rocks, *Geophysics,* **75,** N109–N120.

Holocher, J., Peeters, F., Aeschbach-Hertig, W., Kinzelbach, W. & Kipfer, R., 2003. Kinetic model of gas bubble dissolution in groundwater and its implications for the dissolved gas composition, *Environ. Sci. Technol.,* **37,** 1337–1343.

Jaeger, J. C., Cook, N. G. W. & Zimmerman, R. W., 2007. *Fundamentals of Rock Mechanics,* 4th edn, Blackwell.

Kareem, R., Cubillas, P., Gluyas, J., Bowen, L., Hillier, S. & Greenwell, H., 2017. Multi-technique approach to the petrophysical characterization of Berea sandstone core plugs (Cleveland Quarries, USA), *J. Petrol. Sci.Eng.,* **147,** 436–455.

Kiefer, S. W., 1977. Sound speed in liquid-gas mixtures: water-air and water-steam, *J. geophys. Res.,* **82,** 2895–2904.

Khalid, P., Broseta, D., Nichita, D. V. & Blanco, J., 2014. A modified rock physics model for analysis of seismic signatures of low gas-saturated rocks, *Arab J. Geosci.,* **7,** 3281–3295.

Kurzon, I., Lyakhovsky, V., Navon, O. & Lensky, N. G., 2015. Damping of pressure waves in visco-elastic, saturated bubbly magma, in *Fluid Motions in Volcanic Conduits: A source of Seismic and Acoustic Signals,* Geological Society Special Publications no. 307, pp. 11–31, eds Lane, S. J. & Gilbert, J. S, Geological Society of London.

Krevor, S. C. M., Pini, R., Zuo, L. & Benson, S. M., 2012. Relative permeability and trapping of CO_2 and water in sandstone rocks at reservoir conditions, *Water Resour. Res.,* **48**(2), doi:10.1029/2011WR010859.

Krevor, S., Blunt, M. J., Benson, S. M., Pentland, C. H., Reynolds, C., Al-Menhali, A. & Niu, B., 2015. Capillary trapping for geologic carbon dioxide storage – from pore scale physics to field scale implications, *Int. J. Green. Gas Cont.,* **40,** 221–237.

Landau, L. D. & Lifshitz, E. M., 1989. *Fluid Mechanics,* 2nd edn, Pergamon Press.

Liang, J. -H., McWilliams, J. C., Sullivan, P. P. & Baschek, B., 2011. Modeling bubbles and dissolved gases in the ocean, *J. geophys. Res.,* **116**(C3), doi:10.1029/2010JC006579.

Lissa, S., Ruf, M., Steeb, H. & Quintal, B., 2021. Digital rock physics applied to squirt flow, *Geophysics,* **86**(4), doi:10.1190/geo2020-0731.1.

Lyakhosky, V., Hurwitz, S. & Navon, O., 1996. Bubble growth in rhyolitic melts: experimental and numerical investigation, *Bull. Volcanol.,* **58,** 19–32.

Madonna, C., Almqvist, B. S. G. & Saenger, E. H., 2012. Digital rock physics: numerical prediction of pressure-dependent ultrasonic velocities using micro-CT imaging, *Geophys. J. Int.,* **189,** 1475–1482.

Masson, Y. J. & Pride, S. R., 2007. Poroelastic finite difference modeling of seismic attenuation and dispersion due to mesoscopic-scale heterogeneity, *J. geophys. Res.,* **112**(B3), doi:10.1029/2006JB004592.

Masson, Y. J. & Pride, S. R., 2014. On the correlation between material structure and seismic attenuation anisotropy in porous media, *J. geophys. Res.,* **119,** 2848–2870.

Mavko, G. & Mukerji, T., 1998. Bounds on low-frequency seismic velocities in partially saturated rocks, *Geophysics,* **63,** 918–924.

Mavko, G. & Jizba, D., 1991. Estimating grain-scale fluid effects on velocity dispersion in rocks, *Geophysics,* **56,** 1940–1949.

Mavko, G., Mukerji, T. & Dvorkin, J., 2009. *The Rock Physics Handbook: Tools for Seismic Analysis of Porous Media,* 2nd edn, Cambridge Univ. Press.

Mecredy, R. C. & Hamilton, L. J., 1972. The effects of non-equilibrium heat, mass and momentum transfer on two-phase sound speed, *Int. J. Heat Mass Tran.,* **15,** 61–72.

Mikhaltsevitch, V., Lebedev, M. & Gurevich, B., 2015. A laboratory study of attenuation and dispersion effects in glycerol-saturated Berea sandstone at seismic frequencies, in *Paper presented at the 2015 SEG Annual Meeting,* October 2015, New Orleans, Louisiana.

Mu¨ller, T. M., Gurevich, B. & Lebedev, M., 2010. Seismic wave attenuation and dispersion resulting from wave-induced flow in porous rocks – a review, *Geophysics,* **75,** A147–A164.

Murphy, W. F., Winkler, K. W. & Kleinberg, R. L., 1984. Frame modulus reduction in sedimentary rocks: the effect of adsorption on grain contacts, *Geophys. Res. Lett.,* **1,** 805–808.

Murphy, W. F., 1984. Acoustic measures of partial gas saturation in tight sandstones, *J. geophys. Res.,* **89,** 11 549–11 559.

Murphy, W. F., Winkler, K. W. & Kleinberg, R. L., 1986. Acoustic relaxation in sedimentary rocks: dependence on grain contacts and fluid saturation, *Geophysics,* **51,** 757–766.

Nichita, D. V., Khalid, P. & Broseta, D., 2010. Calculation of isentropic compressibility and sound velocity in two-phase fluids, *Fluid Phase Equilibria,* **291,** 95–102.

Obermann, A., Kraft, T., Larose, E. & Wiemer, S., 2015. Potential of ambient seismic noise techniques to monitor the St. Gallen geothermal site (Switzerland), *J. geophys. Res.,* **120,** 4301–4316.

O'Connell, R. J. & Budiansky, B., 1977. Viscoelastic properties of fluid-saturated cracked solids, *J. geophys. Res.,* **82,** 5719–5735.

O'Connell, R. J. & Budiansky, B., 1978. Measures of dissipation in viscoelastic media, *Geophys. Res. Lett.,* **5,** 5–8.

Onuki, A., 1991. Sound propagation in phase-separating fluids, *Phys. Rev.,* **43,** 6740–6755, .

Picard, D. J. & Bishnoi, P. R., 1987. Calculation of the thermodynamic sound velocity in two-phase multicomponent fluids, *Int. J. Mult. Flow,* **13,** 295–308.

Pimienta, L., Fortin, J. & Guéguen, Y., 2014. Investigation of elastic weakening in limestone and sandstone samples from moisture adsorption, *Geophys. J. Int.,* **199,** 335–347.

Pimienta, L., Borgomano, J. V. M., Fortin, J. & Guéguen, Y., 2016. Modelling the drained/undrained transition: effect of the measuring method and the boundary conditions, *Geophys. Prospect.,* **64,** 1098–1111.

Pimienta, L., Fortin, J. & Guéguen, Y., 2017. New method for measuring compressibility and poroelasticity coefficients in porous and permeable rocks, *J. geophys. Res.,* **122,** 2670–2686.

Pride, S. R., Berryman, J. G. & Harris, J. M., 2004. Seismic attenuation due to wave-induced flow, *J. geophys. Res.,* **109**(B1), doi:10.1029/2003JB002639.

Prosperetti, A., 2015. The speed of sound in a gas-vapour bubbly liquid, *Interface Focus,* **5**(5), doi:10.1098/rsfs.2015.0024.

Quintal, B., Steeb, H., Frehner, M. & Schmalholz, S. M., 2011. Quasi-static finite element modeling of seismic attenuation and dispersion due to wave-induced fluid flow in poroelastic media, *J. geophys. Res.,* **116**(B1), doi:10.1029/2010JB007475.

Quintal, B., Steeb, H., Frehner, M., Schmalholz, S. M. & Saenger, E. H., 2012. Pore fluid effects on S-wave attenuation caused by wave-induced fluid flow, *Geophysics,* **77,** L13–L23.

Quintal, B., Caspari, E., Holliger, K. & Steeb, H., 2019. Numerically quantifying energy loss caused by squirt flow, *Geophys. Prospect.,* **67,** 2196–2212.

Rozhko, A. Y., 2020. Effects of pore fluids on quasi-static shear modulus caused by pore-scale interfacial phenomena, *Geophys. Prospect.,* **68,** 631–656.

Sander, R., 2015. Compilation of Henry's law constants (version 4.0) for water as solvent, *Atmos. Chem. Phys.,* **15,** 4399–4981.

Skempton, A. W., 1954. The pore-pressure coefficients A and B, *Geotechnique,* **4,** 143–147.

Spencer, J. W. & Shine, J., 2016. Seismic wave attenuation and modulus dispersion in sandstones, *Geophysics,* **81,** D211–D231.

Tarokh, A. & Makhnenko, R. Y., 2019. Remarks on the solid and bulk responses on fluid-filled porous rock, *Geophysics,* **84,** 1942–2156.

Teja, A. S. & Rice, P., 1981. Generalized corresponding states method for viscosities of liquid mixtures, *Indust. Eng. Chem. Fundament.,* **20**(1), 77–81.

Tisato, N., Quintal, B., Chapman, S., Podladchikov, Y. & Burg, J. -P., 2015. Bubbles attenuate elastic waves at seismic frequencies: first experimental evidence, *Geophys. Res. Lett.,* **42,** 3880–3887.

Toms, J., Mu¨ller, T. M., Ciz, R. & Gurevich, B., 2006. Comparative review of theoretical models for elastic wave attenuation and dispersion in partially saturated rocks, *Soil Dyn. Earthq. Eng.,* **26,** 548–565.

Voltolini, M., Kwon, T. -H. & Ajo-Franklin, J., 2017. Visualization and prediction of supercritical CO_2 distribution in sandstones during drainage: an in situ synchrotron X-ray micro-computed tomography study, *Int. J. Green. Gas Cont.,* **66,** 230–245.

Wood, A. B., 1955. *A Textbook of Sound,* The MacMillan Company.

Yin, H., Borgomano, J. V. M., Wang, S., Tiennot, M., Fortin, J. & Guéguen, Y., 2019. Fluid substitution and shear weakening in clay-bearing sandstone at seismic frequencies, *J. geophys. Res.,* **124**(2), 1254–1272.

Zimmerman, R. W., Somerton, W. H. & King, M. S., 1986. Compressibility of Porous Rocks, *J. geophys. Res.,* **91,** 12 765–12 777.

APPENDIX

The bulk modulus of the solid matrix (K_s) of sample DoS-A was determined from the volumetric strain measured during hydrostatic loading, where the pore and confining pressures were changed by the same increment (e.g. Zimmerann *et al*. 1986; Pimienta *et al*. 2017):

$$K_s = \left(\frac{\Delta P_c}{\Delta \epsilon_{\text{vol}}} \right)_{P_{\text{eff}}}. \tag{A1}$$

It is assumed that the pore space is fully interconnected, homogenous and isotropic. In addition, the change in pressure must be slow enough for the pore pressure to be uniform throughout the sample.

Two measurements were performed on the water saturated sample DoS-A at a constant effective pressure of 10 MPa and 45 °C. During the first measurement, the sample was unloaded at a rate of 2 Bar min^{-1}, with the confining pressure reducing from 25 to 15 MPa and the pore pressure reducing from 15 to 5 MPa. During the second measurement the sample was loaded at a rate of 0.5 Bar min^{-1}, with the confining pressure increasing from 25 to 30 MPa and the pore pressure increasing from 15 to 20 MPa. Fig. 1(a) shows the volumetric strain with respect to the change in the confining pressure. Included in Fig. 1(a) is the linear regression of the data, where the slope corresponds to K_s. The determined K_s of ∼47 GPa is elevated with respect to the Voigt–Reuss–Hill (VRH) average of 38.5 ± 2 GPa found using the mineral composition of Domengine sandstone by Voltolini *et al*. (2017) (Table A1).

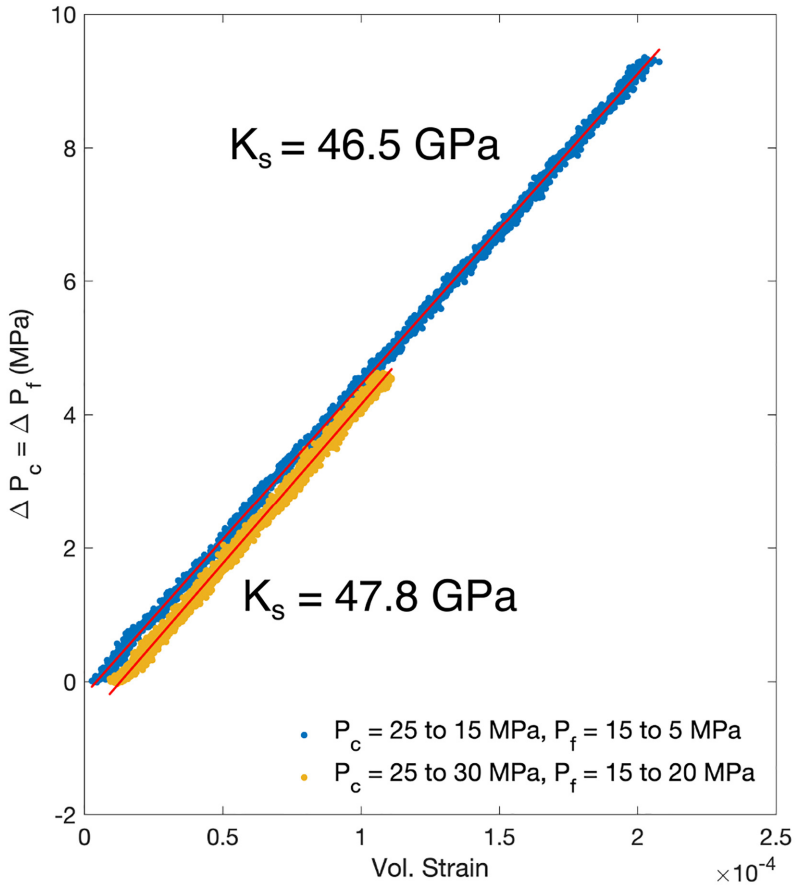

Figure 1A. Change in pressure versus volumetric strain measured on sample DoS-A. The measurements were performed at an effective pressure of 10 MPa and 45 °C. The pore and confining pressures are changed at a rate of 2 and 0.5 Bar min^{-1} for test 1 (blue) and 2 (yellow), respectively. The redlines are the results of a linear regression, the slope of which corresponds to K_s.

Table A1. Physical properties and proportions of minerals.

Mineral	Bulk modulus (GPa)	Weight per cent
Quartz	37[a]	73.8 ± 3 [c]
K-feldspar	58.3[b]	22.7 ± 4 [c]
Smectite	9.3[a]	3.5 ± 2 [c]

[a]Mavko *et al*. (2009), [b] Hacker *et al*. (2003) and [c]Voltolini *et al*. (2017).